Construction, Testing and First Data Analysis with the Cosmic Ray Telescope

Master Degree Thesis in Experimental Particle Physics

by

Øyvind Sætre

Department of Physics and Technology
University of Bergen
Norway

November 15, 2007

Acknowledgements

First of all, I want to thank my wife, Bente, for coping with me these past months and for encouraging words. You rule! Thank you also to my mother, father and two sisters, Ingrid and Randi, for being the best family in the world. Second, a huge thank you to Dr. Lars G. Johansen for all his work and help with the detector. He has been the mastermind of the project. Without him, the CRT would still be a pile of scintillators in a box. Many thanks also to my supervisor, professor Anna Lipniacka, for good input, thorough supervision and patience with an impatient student. Another thank you goes to Hans Torgilstveit, Kåre Slettebakken and Svein Midtun at the workshop for production and helpful insight with all the mechanical parts, and to Magne Munkejord for programming the FPGA on the readout card. Finally, a large thank you to my fellow students for a lot of good input and many enjoyable coffee-breaks. Specially thanks to Øystein Djuvsland for help with the programming bit and CRTGeometry class, and Therese Sjursen for being so cool.

Øyvind Sætre

Contents

Preface

Primary cosmic rays hitting the Earth's atmosphere create a cascade of secondary particles. Only muons and neutrinos reach ground level. The Cosmic Ray Telescope (CRT) is a 16 channel detector using scintillators of a total area of 4 m^2 that can detect muons. The CRT was constructed as the main part of this thesis, and a thorough description of the construction process and testing is given. A first measurement of the mean muon flux and parallel muon event flux has been extracted. In the first step of analysis, the efficiencies of the detector were measured. The theoretical background and processes governing the detector are also described. Finally, some future projects using the CRT are shortly depicted.

Chapter 1

Introduction

The Cosmic Ray Telescope (CRT) is a scintillator detector of a total area of 4 m^2 located at The Institute for Physics and Technology at The University of Bergen. The CRT is designed and constructed to register muons that originate from the decay of mesons created by primary cosmic radiation. Muons are the only hard radiation component that reaches the Earth's surface that are easily detected.

The CRT is primarily designed and commissioned to be used in exercises for undergraduate students, with the possibility that also high school students may participate in simple exercises involving the detector. The theoretical part of the thesis is therefore thought as an introduction to subatomic physics, with emphasis on the processes that are important to understand the setup and functionality of the detector. A short introduction to astrophysics and cosmology is also included to explain the possible origin of cosmic rays. The main part of the thesis describes the construction and testing of the detector and the developement of analysis tools. A first data analysis is also described. The thesis as a whole is thought to be an introduction to and a manual for the detector.

The work involved in this thesis has been diverse, ranging from theoretical studies to computer programming, mechanical production and assembly of components. The better part of our effort has been the actual construction of the detector, and solving the numerous problems that have emerged in the process.

Chapter 2

Theoretical and Historical Background

The Standard Model is a working description of the building blocks of nature and the interactions of these on a microscopic level. In order to understand the processes that govern the detector, it is important to give a general introduction to this theory with emphasis on the interactions and particles that are relevant for the CRT. In addition, it is necessary to give a short introduction to astroparticle physics to understand what we are looking at in the detector. This will cover the history of the Universe and cosmic rays, and the hypotheses on the origin of cosmic radiation.

2.1 Matter Particles and Interactions

Matter consists of quarks and leptons. To our knowledge, quarks and leptons are point like, fundamental particles, with an experimental upper limit on the radius of 10^{-18} m [1]. Both types of particles are fermions, meaning that they have spin 1/2.[1] There are three generations of each, with two particles in each generation. Each matter particle has an associated anti-particle. The anti-particles have opposite quantum numbers of their matter partners. All stable matter is made of particles in the first generation.

Particles interact via four known forces or interactions: the strong, weak, electromagnetic and gravitational interactions. Gravity is neglected in particle physics because it is much weaker than the other three forces. In addition, it is not fully incorporated into the Standard Model because a quantum mechanical description of gravity has not yet been formulated. The interactions have effect on different matter particles: The electromagnetic interaction affects all particles with electric charge, the strong interaction affects all particles with strong charge and the weak interaction affects all known fermions. Experiments have shown that interactions follow many conservation laws[2]. The properties of the matter particles that correspond to these conservation laws are called quantum numbers. There are two

[1] Spin is not due to self-rotation, but is a property of the particle that shows similar mathematical behavior to that of angular momentum. The value of the spin is an integer or half integer multiplied by $\hbar$.

[2] The weak interaction breaks some as explained later.

Particle	Symbol	Electric charge [e]	Mass	Interaction
Photon	γ	0	0 ($< 6 \cdot 10^{-17}$ eV)	Electromagnetic
Z^0-boson	Z^0	0	91.1876 $\pm$ 0.0021 GeV	Weak
$W^{\pm}$-boson	$W^{\pm}$	± 1	80.403 $\pm$ 0.029 GeV	
Gluons	g	0	0	Strong

Table 2.1: Standard Model Boson mediators [3].

categories: quantum numbers associated with space-time symmetries and internal quantum numbers. Examples of quantum numbers are electric charge, baryon number and spin.

The Standard Model states that action at a distance is transmitted by quanta [2]. Therefore, the forces introduced above are mediated by intermediate particles. These are bosons (spin-1 particles). An overview of the intermediate bosons and some properties are given in table 2.1.

2.1.1 Quarks

The quarks come in six flavors, two in each generation: up, down, charm, strange, top and bottom. Flavor is an internal quantum number. A u-quark has up-ness $U = 1$ and an anti-u has $U = -1$. All other quarks have $U = 0$. The same is true for down-ness D, strange-ness S and so on. Quarks have an electric charge of either $\frac{2}{3}e$ or $-\frac{1}{3}e$. In addition, the quarks also carry strong charge, which has been given the name color charge. There are three color charges called red, blue and green with corresponding anti-colors. If all three colors are added or color is added with anti-color, it gives a color-neutral object. Quarks are bound together by the strong interaction in hadrons, either mesons (bosons) or baryons (fermions). Searches for other configurations have given negative results. Mesons and baryons are color-neutral. The configuration is:

$$\text{meson}(q\bar{q})$$
$$\text{baryon}(qqq)$$

The quarks have baryon number $\frac{1}{3}$ and anti-quarks $-\frac{1}{3}$, giving a baryon number $B = 1$ for a baryon, $B = -1$ for an anti-baryon and $B = 0$ for a meson. The mesons and baryons are always configured such that the electric charge of the hadron is an integer value of e (either 0,± 1 or ± 2). Quarks have not been observed to exist freely, implying that they are always bound in hadrons. Therefore, their masses have to be measured indirectly and approximated via theoretical arguments [4]. The quarks and some properties are listed in table 2.2.

2.1.2 Leptons

The leptons, unlike the quarks, can exist as free particles. Each generation has an electrically charged $1e$ lepton and a neutral lepton. The charged leptons are the electron, muon

Particle	Symbol	Electric Charge [e]	Mass
Up	u	$\frac{2}{3}$	1.5-3.0 MeV
Down	d	$-\frac{1}{3}$	3-7 MeV
Charm	c	$\frac{2}{3}$	1.25 $\pm$0.09 GeV
Strange	s	$-\frac{1}{3}$	95 $\pm$25 MeV
Top	t	$\frac{2}{3}$	174.2 $\pm$3.3 GeV
Bottom	b	$-\frac{1}{3}$	4.20 $\pm$0.07 GeV

Table 2.2: Standard Model Quarks [3].

Particle	Symbol	Charge [e]	Mass
Electron	e	-1	0.51099892 $\pm$ 0.00000004 MeV
Electron-neutrino	ν_e	0	< 2 eV
Muon	μ	-1	105.658369 $\pm$ 0.000009 MeV
Muon-neutrino	ν_μ	0	< 2 eV
Tau	τ	-1	1776.99 $\pm$0.29 MeV
Tau-neutrino	ν_τ	0	< 2 eV

Table 2.3: Standard Model Leptons [3].

and tau, and the neutral leptons are the corresponding electron-, muon- and tau-neutrinos. All leptons have baryon number 0 and no quark flavor ($U = D = S = ... = 0$). Instead, they have lepton numbers L_e, L_μ and L_τ. The electron and electron neutrino have $L_e = 1$ and $L_\mu = L_\tau = 0$, and the other leptons have L in analogy with this. The anti-particles have lepton numbers of opposite sign. All quarks have lepton numbers 0. The leptons and some properties are given in table 2.3.

Neutrinos were initially considered to be massless, but recent studies of neutrinos have revealed that they oscillate (i.e. change flavor "by themselves") [5]. This is only possible if they have non-zero mass. Presently, it is only possible to measure the squares of the difference between the neutrino masses of two generations. No direct value of the masses can yet be given, only upper limits.

2.1.3 Interactions

We can visualize an interaction with a Feynman diagram, which connects particles that interact with the intermediate boson that is transmitting the interaction. Two examples are given in figure 2.1.

We see that a real interaction has a minimum of two vertices (two "contact-points"); one where the boson "starts" and one where it "stops". These vertices are governed by parameters called coupling-constants. The bosons can couple to the various elementary particles given in table 2.2 and 2.3, and the strength of the interaction between particle and boson mediator is determined by the coupling constant. In the quantum theory of interactions, the coupling is proportional to the charge of the interaction and specific for

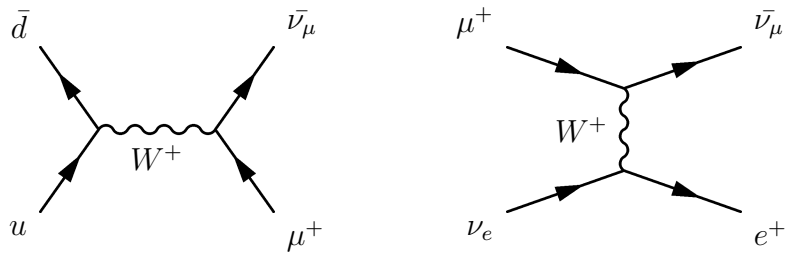

Figure 2.1: Charged pion (π^+)and anti-muon (μ^+) decay

the particular fermions. We speak of electric, weak and strong charge. Thus, a boson does not always couple with the same strength to all particles, e.g. the coupling between a γ and a u-quark is different from the coupling between a γ and a b-quark.

If an interaction is sufficiently weak (the coupling constant is sufficiently small), perturbation theory can be employed. In perturbation theory, we assume that the Hamiltonian of the interaction deviates only slightly from the Hamiltonian of a free system. In it's simplest form (to first order), an interaction can be described by a relation named Fermi's Golden Rule [6]: The transition rate ω from an initial state $|\alpha\rangle$ to a final state $|\beta\rangle$ is given by

$$\omega_{\beta\alpha} = \frac{2\pi}{\hbar} \left|\langle\beta|H_{\text{int}}|\alpha\rangle\right|^2 \rho(E) \tag{2.1}$$

where H_{int} is the interaction Hamiltonian and $\rho(E)$ is the density-of-states factor. The interaction Hamiltonian is made up of the coupling constants and the boson propagator, while the $|\alpha\rangle$ and $|\beta\rangle$ are the quantum mechanical descriptions (eigenstates) of the initial and final states. The density-of-states factor quantifies how many particles the final state can hold per unit of it's energy.

Quantum theory states that all interaction modes that are not forbidden, are possible. If an interaction can result in several final states, the transition rate is a sum over all possible final states. We then have to find all the possible matrix elements $|\langle\beta|H_{\text{int}}|\alpha\rangle|$ that give the transition $|\alpha\rangle \rightarrow |\beta\rangle$. The total transition rate is found as the sum of transition rates to the various final states. For most reactions, only one or a few final states dominate the total transition rate. The rest are highly unlikely.

2.1.4 The Electromagnetic Interaction

The electromagnetic interaction affects all particles with an electric charge. Thus, both charged leptons and quarks are affected. The mediator of the interaction is the photon, a massless particle without electric charge. Nearly all known quantum numbers are conserved in the electromagnetic interaction.

The coupling constant of the electromagnetic interaction is the electron charge e. As we see in equation 2.1, the interaction Hamiltonian and therefore the coupling constant enters squared. A dimensionless constant is introduced:

$$\alpha \equiv \frac{e^2}{\hbar c} \approx \frac{1}{137} \tag{2.2}$$

This constant is called the fine-structure constant. In perturbation theory it is a measure of the strength of the electromagnetic interaction.

Using perturbation theory on the electromagnetic interaction has been outstandingly successful in quantum electrodynamics (QED) [7]. This has led to a theoretical description of the interaction that has been verified to very high precision by experiments.

2.1.5 The Strong Interaction

The strong interaction affects all matter particles with color charge, which are the quarks. It is mediated by massless particles called gluons. Unlike photons, who do not carry electric charge, gluons carry color and anti-color. All known quantum numbers are conserved in the strong interaction.

The strong interaction can be studied by looking at quarks bound in hadrons. At long distances, the strong interaction is very complex. One of the reasons for this are gluon-gluon interactions that take place in the field between the quarks. This gives rise to non-neglectable higher order terms that prohibit the use of perturbation theory. An accurate and satisfying theory describing the interactions at long distances has not yet been constructed. At small distances or high energies, this changes, and the strong interaction can be approximated by first-order processes, allowing the use of perturbation theory in a similar way as for the electromagnetic interaction. A coupling α_s in analogy to the fine-structure constant α can be calculated. Because the gluons can carry color, α_s depends on the momentum transfer or distance probed, becoming smaller when the momentum transfer becomes larger.[3] For large distances (low energies), α_s grows large due to the gluon-gluon interactions. In the low-energy theory (at large distances), the strong interaction can be described as mediated by meson exchanges.

We can give a phenomenological description of quark confinement in a simplified model. If something tries to separate two quarks in a meson, the field between them gets longer, increasing the energy of the field. If the quarks are separated enough, the gluon field has enough energy to create real $q\bar{q}$ pairs. This is more energetically favorable than having a stretched field. The quarks from the initial meson combine with the quarks from the $q\bar{q}$ pair, resulting in mesons. This is a consequence of the gluons carrying color charge. It is one of the mechanisms responsible for quarks not being observed as free particles (confinement), and limits the range of the strong interaction to $\sim 10^{-15}$ m despite the gluons being massless. The phenomenon described above is called fragmentation.

2.1.6 The Weak Interaction

The weak interaction is the only interaction that affects all standard model matter particles. It is mediated by massive vector bosons, the Z^0 and $W^{\pm}$. Since the Z^0 is neutral while the $W^{\pm}$ have electric charge, we speak of neutral currents (NC) and charged currents

[3] In comparison, the fine-structure constant increases slightly at high energies.

(CC). Because of the large mass of the bosons (table 2.1), the effective range of the weak interaction is very small. This comes as a result of Heisenberg's uncertainty relation

$$\Delta E \Delta t \geq \frac{\hbar}{2} \tag{2.3}$$

Equation 2.3 is one of the fundamental laws of quantum mechanics. The boson mediators are virtual. The energy that is needed to create their masses, is "borrowed" from the vacuum energy ($\Delta E = \Delta M$). In this situation, the lifetime τ follows

$$\tau \leq \frac{\hbar}{2\Delta M} \tag{2.4}$$

Since the bosons are so massive, they have very short lifetimes and thus can only mediate interactions over very short distances ($\sim 10^{-18}$ m). Therefore, the weak interaction appears much weaker than the strong and electromagnetic interactions. At low energies, it is only significant when it is the only allowed mode.

Since all matter particles interact weakly, they all must have weak charge. In low-energy interactions like the muon-decay, the weak coupling g (i.e. the weak charge) is replaced by a new coupling G_F called the Fermi coupling [2]:

$$G_F = \sqrt{2} 4\pi g^2 {R_W}^2 = \sqrt{2} 4\pi \left(\frac{\hbar}{m_W c} \right)^2 g^2 = 0.896 \cdot 10^{-4} \text{MeV/fm}^3 \tag{2.5}$$

The parallel to the fine-structure constant (equation 2.2) is given by:

$$\alpha_W = \frac{g^2}{\hbar c} = \frac{1}{\sqrt{2} \cdot 4\pi} \frac{1}{\hbar c} \left(\frac{m_W c}{\hbar} \right)^2 G \approx \frac{1}{240} \tag{2.6}$$

with boson mediator mass $m_W \approx 80$ GeV. We see that the strength of the interaction is of the same order of magnitude as the electromagnetic, showing that the weakness of the weak interaction is due to the massive bosons as already mentioned. The similarities in strength was one of the reasons that led to a quantum mechanical unification of the electromagnetic and weak interactions in the electroweak theory.

Unlike the strong and electromagnetic interactions, not all quantum numbers are conserved by the weak interaction. The weak interaction does not conserve flavor, making it possible for a quark to change flavor and/or generation. Hence, all quark decays from one generation to another are mediated by the weak interaction. It is also the only interaction that allows charged leptons to change into neutrinos (a lepton "flavor" change). Thus, all charged lepton decays go via the weak interaction. The decay conserves lepton number.

There is strong experimental evidence that neutrinos oscillate, meaning that they change from one generation to another. This implies that for these oscillations, lepton number is not conserved. This violation of lepton number is small. In all weak processes involving other particles than neutrinos, we can treat lepton number as conserved.

The spin of a matter particle can be projected in two directions; either parallel to ("right-handed") or anti-parallel to ("left-handed") the momentum. This projection is called the helicity of the particle. A quantum mechanical operation called parity (P-parity) changes the direction of the momentum and position vectors, leaving the spin and angular momentum unchanged. This turns a left-handed state into a right-handed state and visa versa. Quarks and charged leptons exist as both right-handed and left-handed in nature. The neutrinos do not. All experimental evidence show that neutrinos are always left-handed, while anti-neutrinos are right-handed. This means that the weak interaction does not conserve parity. In fact, it violates parity maximally.

Another operator is charge conjugation (C-parity). The C-operator changes all the internal quantum numbers of a particle, turning it into it's anti-particle while leaving all spatial properties (spin, momentum, position etc.) unchanged. Again, charge conjugation is violated by the weak interaction because of the neutrinos. We will see what this P- and C-violation means by looking at the charged pion and muon decays.

2.1.7 Charged Pion decay

Charged pions have quark configuration $u\bar{d}$ (π^+) or $\bar{u}d$ (π^-). Their decay mode is totally dominated (99.99 %) by

$$\begin{aligned} \pi^+ &\rightarrow \mu^+ + \nu_\mu \\ \pi^- &\rightarrow \mu^- + \bar{\nu_\mu} \end{aligned} \tag{2.7}$$

A Feynman diagram of the π^+-decay is given in figure 2.1. The pion-decay is a two-body decay resulting in a muon and a muon-neutrino. Because energy and momentum is conserved, the muon and muon-neutrino have well-defined energies. We consider a π^+-decay where, for simplicity, the pion is at rest. Since the neutrino must be left-handed, it means that the anti-muon must also be left-handed in order to have spin conservation (the pion has spin 0). If we do a parity operation on the system, we get an illegal mode containing a left-handed anti-neutrino. Experiments measuring the polarization of the anti-muons coming from π^+-decays, have only found left-handed anti-muons [4]. If parity was conserved, the two modes should have equal probabilities, meaning that measuring polarization would give 50 % right-handed and 50 % left-handed states. Since the muon spin is polarized totally in one direction, we speak of maximal P-violation. In analogy to the P-operation, if we let C operate on the π^+-decay, we get a π^--decay with a left-handed muon and anti-neutrino. This mode is forbidden and is not observed in nature. This means that also C-parity is violated maximally because only one mode is allowed. For positive pions with non-zero momentum, we get right-handed anti-muons.

Individually, we see that P- and C-parity are maximally violated in weak interactions involving neutrinos. If we combine the two operations, we get a CP-operation. Experiments have shown that CP is also violated, but that the violation is small. CP-violation was first

[4] In a π^--decay, only right-handed muons are observed.

observed in kaon-decays. For the pion decay, it is negligible, and for all practical purposes we can look at CP as conserved in this decay.

2.1.8 Muon decay

The muon decays into an electron. Lepton number conservation dictates that the electron is accompanied by a muon-neutrino and an electron anti-neutrino. The muon and anti-muon decay modes given under are totally dominating ($\approx 100\%$):

$$\begin{aligned} \mu^- &\rightarrow e^- + \nu_\mu + \bar{\nu_e} \\ \mu^+ &\rightarrow e^+ + \bar{\nu_\mu} + \nu_e \end{aligned} \tag{2.8}$$

In it's rest system, the muon has a lifetime of $\sim 2.2\mu$s in vacuum.

The muon-decay is a three-body decay. Because the energy and momentum of the initial muon can be divided between three particles, their energies are given by a continuous distribution. The muon rest mass is $\sim 106\text{MeV/c}^2$, over 200 times larger than the mass of the electron; the neutrinos are considered massless. Special relativity states that mass is a form of energy and that a particle has energy

$$E = \sqrt{(pc)^2 + (mc^2)^2} \tag{2.9}$$

where p is the momentum and m is the rest mass of the particle. In order to have energy conservation, most of the muon's mass is converted to kinetic energy in the decay products, giving them relativistic energies. The maximum energy the electron can have is

$$E = \frac{m_\mu}{2}\left(1 + \frac{m_e^2}{m_\mu^2}\right) \tag{2.10}$$

giving

$$\beta \equiv \frac{v}{c} = \frac{pc}{E} \simeq 1 \tag{2.11}$$

In this situation, the electrons preferentially are emitted in the opposite direction of the two neutrinos. If we look at a muon at rest, we can project the muon spin either parallel or anti-parallel to the electron momentum. The neutrinos have opposite spins, which cancel each other. In order to have spin conservation, the electron spin must have the same projection as the muon. This gives two possible modes: the electron is emitted parallel to the muon spin (right-handed electron) or anti-parallel to the muon spin (left-handed electron). If parity was conserved, the two should occur with approximately the same rate, but experiments show that the first mode is suppressed by factors which are typically of the order

$$(1 - \beta) \approx \frac{m_e}{2E^2}, \tag{2.12}$$

where m is the appropriate fermion mass [4]. It appears that in the relativistic limit, only left-handed charged fermions are allowed, and their helicity behavior is similar to that of the

neutrinos. As in the pion-decay, C and P-parity are maximally violated, while CP-violation is negligible because of the small masses involved.

Most particles studied in particle physics are not stable. Because they are unstable, their mass is not well-defined either. If produced in an accelerator [5], the probability of producing such an unstable particle is given by a Breit-Wigner distribution:

$$f(E) \sim \frac{1}{(E^2 - M^2)^2 + M^2\Gamma^2} \tag{2.13}$$

with center-of-mass energy E, resonance mass M and full width at half maximum (FWHM) Γ. The most probable mass is the peak of the Breit-Wigner curve, called the resonance, but particles are produced in an interval of E, not for just one exact value. The lifetime τ of a particle is related to the width Γ by:

$$\tau = \frac{1}{\Gamma} \tag{2.14}$$

allowing the lifetime to be taken from the distribution of the particle. It is obvious that a narrower resonance (e.g. a more well-defined mass) gives a longer lifetime. The muon has a relatively long lifetime, giving it a narrow resonance and almost well-defined mass.

2.2 Cosmic radiation

Cosmic rays are charged particles that come from sources in the Universe and impinge the Earth's atmosphere. As in stellar abundance determinations, hydrogen nuclei (protons) are by far the most abundant component, constituting about 90 percent of all the cosmic ray nuclei. Another nine percent are helium nuclei, while the remainder is divided among heavier elements [8]. In addition to nuclei, a small fraction of the cosmic rays consist of other charged particles. These are mostly electrons, and more rarely anti-particles like anti-protons and positrons. The observed energies of cosmic rays range over 14 orders of magnitude, from 10^6 eV - 10^{20} eV. Hitting the atmosphere, the cosmic rays interact strongly with gas-nuclei in the air, dividing it's energy among several nuclei which are shoved earthward. These, in turn, often hit other gas nuclei, creating a cascade of lower-energy particles that eventually reach the Earth's surface as a cosmic ray shower [9]. The total cosmic ray nuclei flux as a function of the energy and descriptions of a cascade induced by cosmic rays are given in figures 2.2 and 2.3.

In addition to charged particles, neutral particles hit the Earth's atmosphere. The largest part is made of neutrons, high-energy gamma-rays and neutrinos. The neutrons and gamma-rays can induce cascades like the charged particles, while the cross-section for neutrino-interactions is so small that most neutrinos pass through the Earth and everything on it's surface without anything happening. For this reason, neutrinos are not interesting for the CRT. Because of their penetrating power, the neutrinos can give much valuable information. The trouble is that they are hard to detect.

[5] For instance by colliding electrons and positrons head on.

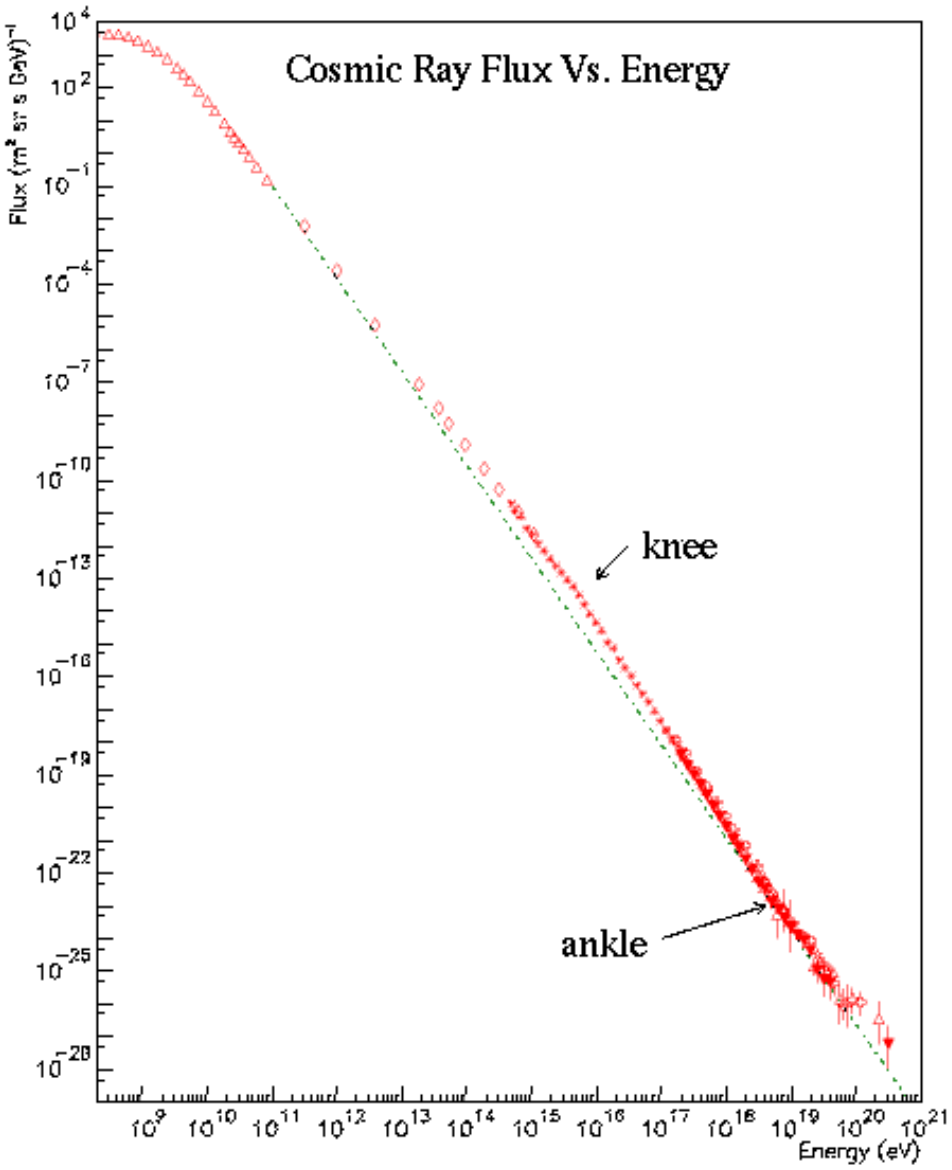

Figure 2.2: The total flux of primary cosmic nuclei as a function of the energy [10]. The total flux seems to follow a power law, with two changes in the steepness; it becomes steeper at "the knee" at $10^{15} - 10^{16}$ eV, and flattens at "the ankle" at $\sim 10^{19}$ eV.

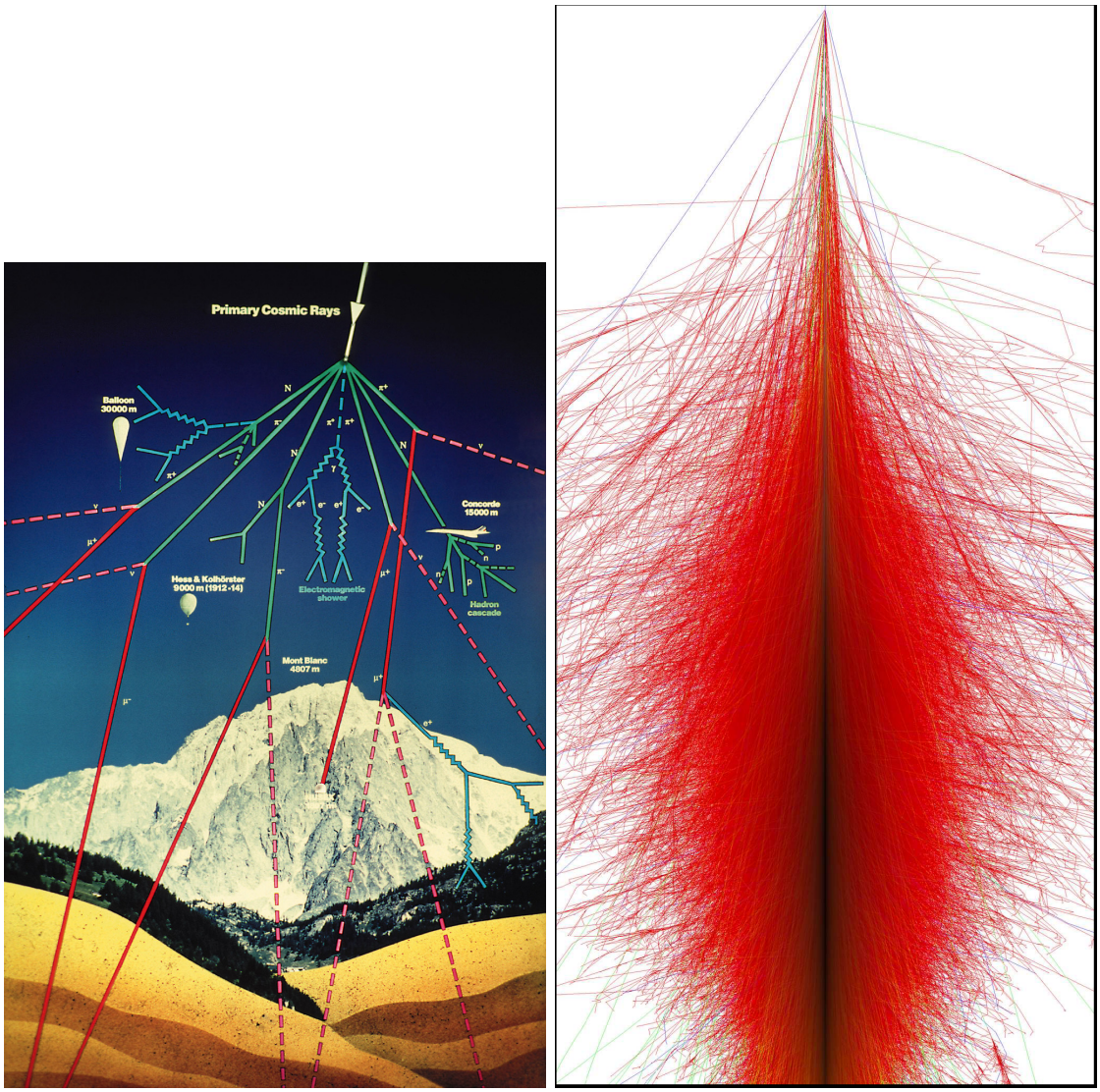

(a) A schematic description of a cascade induced by cosmic rays, implying the different particles that can be produced. Notice that muons are the only particles able to reach the ground. Image courtesy of CERN.

(b) A simulated air shower induced by a 10^{15} eV proton [11]. The top of the shower is the primary interaction point, and the bottom is the ground. We see that such an event produces a vast amount of particles. Notice that the shower maximum is well above ground level.

Figure 2.3: Two figures showing cascades induced by primary cosmic nuclei.

2.2.1 Big Bang and the Universe

The dominating theory on the origin and development of the Universe is the Big Bang theory. In this theory, the Universe emerged from a state of immense temperature and density. Observations suggest that this happened about 13.8 billion years ago [9]. In the first fraction of time ($0-10^{-43}$ s called the Planck era), the energy density and temperature was so extremely large that all the four fundamental forces could have been united. This was followed by a grand unified epoch in which gravity was separated from the other three interactions. The strong force then decoupled from the electroweak, and an inflation phase followed after about $10^{-35} - 10^{-32}$ s. In the inflation phase, the Universe entered a very odd and unstable high-energy state that physicists call "the false vacuum". For a short while, empty space acquired an enormous pressure, which temporarily overcame the pull of gravity and accelerated the expansion of the Universe exponentially. The inflation period lasted a mere 10^{-32} s, but increased the size of the Universe by the incredible factor of about 10^{50} [12]. During the inflation period, the temperature in the Universe dropped due to the expansion. When the inflation stopped, the Universe reheated. It was dominated by radiation, but quarks, electrons and neutrinos were formed in a process called baryogenesis. This process for unknown reasons did not conserve baryon number, resulting in a slightly higher production of particles than anti-particles. When the baryogenesis was over (after about 10^{-12} s), the Universe consisted of a quark-gluon plasma.

In the following period ($10^{-12}-10^{-6}$ s), the electromagnetic and weak forces were separated. In this electroweak symmetry breaking, it is believed that the particles acquired mass via the Higgs mechanism. The neutrinos decoupled and started traveling around freely. The electroweak period was followed by a hadron epoch ($10^{-6}-10^{-2}$ s) in which the quark-gluon plasma was cooled enough to allow the formation of hadrons. Additional cooling lead to the formation of nucleons (nucleosynthesis from 1 s - 3 min). After this, the temperature of the Universe dropped so much that nuclear fusion no longer was possible.

The Universe continued to expand adiabatically, with the temperature dropping as the volume expanded. After 70 000 years, the non-relativistic matter density was equal to that of relativistic radiation. After 380 000 years, the temperature was so low ($\sim$ 3000 K) that electrons and nucleons could form neutral atoms. This is called recombination. Before this, the radiation was so energetic that it kept matter ionized. A very important consequence of recombination is that the radiation was decoupled from matter. This radiation relic can be measured today as a $\sim$ 2.7 K cosmic microwave background (CMB) forming a perfect black-body spectrum. The CMB is almost perfectly isotropic with small anisotropic variations of the order $\frac{1}{100000}$ or smaller. Both the CMB and it's minor anisotropies were predicted by the Big Bang theory and are maybe the strongest arguments for this theory being correct.

When neutral matter was formed, the density was almost uniform, with only slight variations. Because of these variations, gravitational forces slowly formed clumps of matter. After millions and billions of years, clumps with large enough densities and masses obtained temperatures high enough for fusion processes to occur due to gravitational pressure. This gave rise to early super-heavy stars, consisting of non-metallic matter. Because of gravita-

tional collapse, these formed quasars, re-ionizing the surrounding Universe due to intense electromagnetic radiation. Continuing gravitational forces led to the formation of the structures we observe in the Universe today; stars (where a variety of sizes and types exist), galaxies and clusters of galaxies. Recent studies show that this formation of baryonic structures in the Universe was dependent on non-baryonic, dark matter [6]. While the true nature of dark matter remains uncertain, it's defining property is the fact that it interacts only very weakly with both normal matter and radiation. Consequently, clumps of dark matter were unaffected by the radiation background and began to grow as soon as matter first began to dominate the cosmic density [12]. When neutral baryonic matter was formed, it was affected by the already formed clumps of dark matter by gravitational forces.

The areas between galaxies (intergalactic space) have very low matter density and are very close to vacuum. The areas between stars are called the interstellar medium (ISM), with densities of thousands to several millions of that of the intergalactic space. The Universe has always been and is still expanding. A graphical summary of the Big Bang theory is given in figure 2.4.

In recent years, large accelerator experiments have been carried out in particle- and nuclear physics. With increasing energies available, these experiments have made it possible to study and confirm the Big Bang theory up to a fraction of a second after the start.

2.2.2 Star formation and life

Stars are luminous objects observed in the Universe. They are formed in galaxies by the gravitational collapse of molecular clouds, areas of the ISM which contain molecules. The collapse results in a rise in the temperature, and the matter is turned into a plasma of ionized nuclei and electrons. The nuclei are mostly hydrogen. If the collapsing mass is large enough, the temperature in the core gets high enough for nuclear fusion processes turning hydrogen into helium to start. This process counteracts a further gravitational collapse, stabilizing the star in a hydrostatic equilibrium; the pressure outward from fusion radiation is equal to that of the matter pressing inward. The star continues in this steady state for most of what is called it's main sequence, burning hydrogen and releasing an approximately constant flow of energy until most of the hydrogen fuel in the core is exhausted.

When the main sequence is over, a star changes dramatically. First, the outer layers expand and cool. Hydrogen fusion continues in a layer around the core, filling the core with more and more helium. For stars with mass $\leq 1.5M_{\odot}$ (where $M_{\odot}$ is the mass of the Sun), the temperature does not get high enough for other fusion processes to initiate. When the helium core gets too big, the hydrogen fusion cannot support it anymore and it contracts to a white dwarf. This is a massive star with about the same radius as the Earth. The critical enclosed core mass for this contraction is the Chandrasekhar mass $M_{Ch} \simeq 1.4M_{\odot}$ [13].

---

[6] Baryonic dark matter, like planets, dust and so on have so low abundance that it is negligible when looking at the Universe as a whole. In the following, when speaking of dark matter, we refer to non-baryonic dark matter.

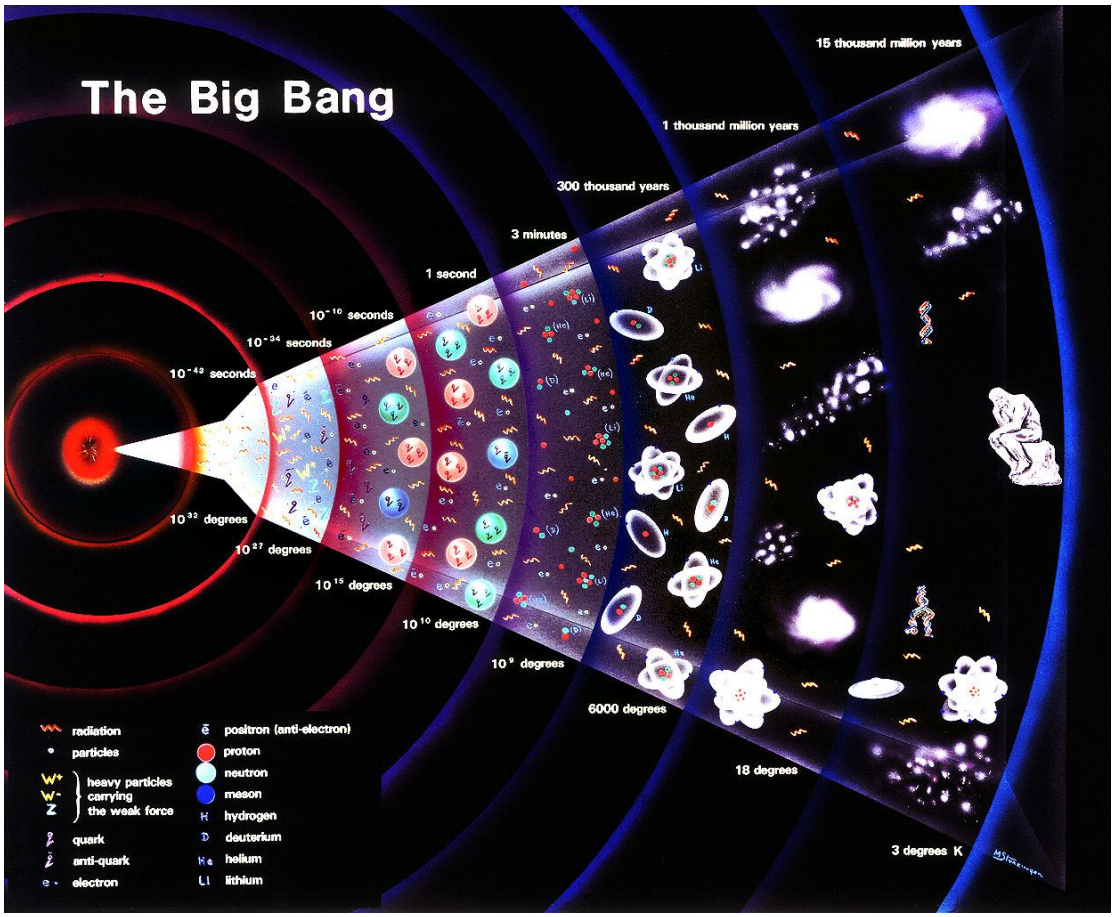

Figure 2.4: A graphical summary of the history of the Universe from the start until today. The summary shows the different phases, what particles and radiation was present and what the relative size of the Universe was. The temperature in the Universe is also indicated, and can be transformed to energy via a linear dependence. Thus, 10^{27} K corresponds to 10^{14} GeV, 10^{15} K to 100 GeV and so on.

For stars with mass many times $M_\odot$, the temperature in the core becomes high enough to initiate higher fusion processes when the hydrogen is exhausted, starting with helium fusing to carbon and oxygen. When the helium fuel is exhausted, higher fusion processes can occur, again starting outside the core. The initial mass of the star decides how heavy elements can be fused. Each time the star changes fuel, the core is contracted, raising the density and the temperature and reducing the radius. For massive stars larger than 9 $M_\odot$, the fusion processes go all the way up to iron. Iron is the most tightly bound nuclei. Fusion of iron to heavier elements would therefore consume energy instead of releasing energy. Along the way, the temperature has exceeded 1 billion degrees, enabling energy to be transported out of the star by neutrinos. Because they have a very low interaction rate with the stellar matter, this reduces the hydrostatic pressure. In addition, disintegration of heavy nuclei and deleptonization further contribute to lowering the pressure outward and

raising the gravitational pressure inward. The evolution of the star goes more and more rapidly.

The steady reduction of hydrostatic pressure reaches a point where the fusion processes no longer can support the core's mass. The core collapses. The radius is reduced from several thousand kilometers to about 50 kilometers in about one second, leading to a nuclear density exceeding 10^{14} g/cm^3. The extreme contraction must be re-adjusted. This happens when the inner part of the core bounces back and meets the rest of the core that is still falling in, causing a shock-wave to propagate through all the matter of the star (stellar matter). This shock carries extreme amounts of energy, and therefore heats and ejects the matter it passes with high velocities. The collapse and shock are what we call a supernova explosion. After the shock, the core is still very hot, and the outer layers maintain high temperatures for thousands of years in a so-called supernova remnant. If the core mass was $< 4M_\odot$, the remainder continues as a neutron star. If the mass exceeded 4 $M_\odot$, the gravitational forces are so great that they turn the core into a black hole.

2.2.3 History of cosmic rays

In 1896, Henry Becquerel by accident discovered radioactivity. The source was uranium salts, and the radiation was characterized by it's ionizing ability. In the following years, measurements of radioactivity were carried out at different locations on the Earth's surface and several hundred meters above it. As the radiation seemed to be reduced with the height above ground, it was assumed that the radiation was solely due to radioactive sources in the Earth itself. In 1912, Victor Hess sent three balloons carrying ionization measuring equipment to a height of 5300 meters. He discovered that at this height, the radiation was approximately four times more ionizing than at ground level. The only explanation he could find was that highly penetrating radiation must be entering the Earths atmosphere from above. He called this radiation "cosmic rays".

The next decade after Hess' discovery, it was generally believed that the cosmic rays were gamma-rays (high-energy photons) and secondary electrons produced by Compton scattering. Then, from 1927-1937, various experiments showed that the radiation at ground level consisted of a "soft" (non-penetrating) and a "hard" (highly penetrating) component. The soft component consisted of electrons and photons, while the hard component was named muons. Initially, the muons were believed to be the mediator of the low-energy strong interaction mentioned earlier. Experiments showed that the muon did not interact strongly, ruling out this possibility. The solution to the problem came in 1947 with the discovery of the pion. Studies of the pion- and muon decays showed that the particles observed at ground level were in fact not the particles that entered the atmosphere primarily.

In 1937, Pierre Auger found that many particles reach the ground at the same time, sometimes over a large area. A closer inspection led to the conclusion that primary cosmic rays interacting with nuclei in the atmosphere, produced showers of secondary particles that reached the ground. It was later shown that the size of the shower was proportional

to the energy of the primary ray. In 1948, Melvin B. Gotlied and James Van Allen were able to send emulsion plates to the top of the atmosphere. These showed that the primary radiation hitting the atmosphere consisted mostly of protons, with some helium nuclei and a fraction of heavier nuclei. A number of studies both at ground level and higher up in the atmosphere, have given extensive knowledge of cosmic rays in the atmosphere.

Almost one century after their discovery, we have no definitive models about the origin, acceleration and propagation process of cosmic rays [14]. Several models and theories have been suggested. We can roughly divide the cosmic rays into two categories; galactic and extra-galactic cosmic rays.

2.2.4 Galactic Cosmic Rays

The Earth is situated in a galaxy called the Milky Way. The galactic magnetic field (with an estimated strength of 3 to 6 $\cdot 10^{-6}$ Gauss [8]) works as a trap for particles below energies of $\sim 10^{15}$ eV. All cosmic rays below this energy are therefore called Galactic Cosmic Rays (GCRs); they are confined within the galaxy. One of the most probable and most studied theories on the origin of GCRs names supernovas as a probable source. When the stellar matter in the supernova hits the interstellar gas, it produces a shock front that heats the gas to many million kelvin, turning it into a plasma. This shock front seems to play an important role in the particle acceleration. The remnant of the supernova, consisting of gas and clouds of magnetic fields, persists for thousands of years after the explosion. Particles trapped in the supernova remnant can be accelerated to high energies via random collisions with the magnetic fields. Given enough energy, these particles can escape the supernova remnant as GCRs. The possible size of the remnant and it's magnetic fields sets an upper limit of $\sim 10^{15}$ eV on the energies the escaping particles can acquire. This corresponds to the area above the knee in figure 2.2. The GCRs are distorted on their journey through the galaxy by the galactic, solar and Earth's magnetic fields. Therefore, we can not directly find out what direction they came from, as they are almost isotropically distributed and follow the magnetic lines of the galactic magnetic field [8].

Cosmic rays of energies below 10 GeV come mainly from the Sun. Their flux is affected by solar flairs, solar wind and the magnetic fields of both the Earth and Sun. They also do not have enough energy to produce particles observable at the Earth's surface when colliding with the atmosphere. Most of them do not even reach the atmosphere, but are deflected by the geomagnetic field. For that reason, they are not interesting for this project.

2.2.5 Extragalactic and Ultra-high-energy Cosmic Rays

The energy limit set on GCRs, suggests that cosmic rays of higher energies come from galaxies outside our own. Their sources and acceleration mechanisms are in no way determined. Several theories have been suggested. In analogy to the supernova remnant theory, it is believed that also extragalactic cosmic rays may be accelerated through electromagnetic processes. These include nonstandard supernova remnants, gamma ray bursts and

black holes, quasars and active galactic nuclei.[7] Galaxies or galaxy clusters colliding are also a possibility. The ultra-high energy cosmic rays (UHECRs) are particles between the knee and the ankle in figure 2.2. For the most energetic particles, the cosmic magnetic and gravitational fields would have little influence, maybe allowing a trace to their origin.

Particles with the highest energies measured (the area above the ankle in figure 2.2) are one of the big mysteries in astrophysics. Ultra high energy protons, according to current estimates and measurements of cross-sections, interact with the cosmic microwave background radiation (CMBR) and lose energy by photo-pion production. For this reason, 10^{20} eV and above protons would be strongly attenuated over distances of a few tens of Mpc [8]. This leads to a theoretical cut-off in the spectrum below 10^{20} eV, the so called Greisen-Zatsepin-Kuzmin(GZK) cut-off [15]. Similar constraints are found for heavy nuclei interacting with the intergalactic infrared background radiation, limiting their range to about 100 Mpc [16]. At these distances from Earth, no possible candidates (galactic or extragalactic) of the type described above exist for production of particles with these energies. Thus, cosmic rays coming from far away sources with energies above this limit, should lose energy before they reach the Earths atmosphere. The observation of several particles with energies exceeding 10^{20} eV can point to new physics beyond the theories presently governing particle physics. Several suggestions have been made. One of the more interesting names dark matter as a possible source of these UHECRs.

Only $\sim$ 4 % of the Universe is made up of hadronic and leptonic ("visible") matter. The rest is dark matter ($\sim$ 22 %) and dark energy ($\sim$ 74 %) [17]. This composition is based on measuring the acceleration of the Universe, the rotational speed of stars inside galaxies, the speed of galaxies compared to each other and the temperature of the cosmic background radiation. Theories for dark matter are presently studied, while dark energy is a complete mystery. The UHECRs are proposed to be the either the decay products [18] or the result of collisional annihilation [19] of super-heavy dark matter particles. If dark matter is indeed the source of the ultra-high-energy cosmic rays, we may be able to learn new physics by studying cosmic rays. The biggest limitation is the extremely low rate of these particles, and so far not enough particles have been detected to give satisfying statistics. The low flux of such particles also rules out the possibility of direct detection. They have to be reconstructed by looking at the cascades of secondary particles they induce. This contributes to higher uncertainties.

2.2.6 Cascades induced by cosmic rays

Cosmic rays entering the Earth's atmosphere will usually collide with nucleons in the atmospheric gas (e.g. oxygen or nitrogen) and produce secondary particles in hadronic interactions. The secondary particles are mostly pions or kaons. Neutral pions decay almost

[7] Sources of this kind have been detected inside our galaxy, for instance in the galactic nuclei, allowing the possibility that some of the extragalactic cosmic rays in fact have galactic origin. The reason we call them extragalactic is because they can escape the galaxy's magnetic field.

[8] 1 pc = 30.857 $\cdot 10^{12}$ km = 3.2616 light years

instantly to two photons. These photons can create particle - anti-particle pairs. Charged pions have longer lifetime and can either decay into muons and neutrinos or collide with gas-molecules producing another set of particles. The kaon decays mostly to either pions or muons. Repeated collisions and decays lead to a cascade (or shower) of particles. With each collision or decay, the energy of the particles is reduced. For the highest energies, a cosmic ray particle can create a shower containing billions of secondary particles.

The cascade is produced via hadronic processes and spreads out in a cone shape. By measuring the width and flux of the cone hitting Earth, it is possible to retrieve information about the primary particle. For the most energetic particles, the cone can cover an area of 25 km^2 [20]. The nuclear interactions are complicated. In practice, this means that two primary particles with the exact same properties can give rise to two very different showers. The reconstruction of cosmic showers therefore relies heavily on simulations using Monte Carlo methods. The observed air-shower features are compared to shower models that assist the derivation of the primary particle energy and type [13]. Because of the uncertainties in the parameters governing the strong interaction, the reconstruction of a shower and corresponding initial particle is derived with considerable systematic uncertainties. The size of the showers and the rarity of the very high energy cases also demands large detectors or arrays of detectors covering areas of several square kilometers.

The muon (and by muon we speak of both muons and anti-muons) is the only charged hard component produced in a cosmic ray shower that has long enough mean lifetime to reach the Earth's surface. Measurements set the mean lifetime of the muon to 2.2 μs in it's rest-frame, and relativistic muons can therefore reach the Earth because of a relativistic phenomenon known as time dilation: The lifetime in the lab-frame τ_{lab} is related to the lifetime τ in the rest-frame of the muon by:

$$\tau_{\text{lab}} = \gamma\tau \qquad , \qquad \gamma = \frac{1}{\sqrt{1 - \left(\frac{v}{c}\right)^2}} \tag{2.15}$$

Thus, muons traveling at relativistic speeds, have a longer lifetime in the lab-frame. The higher the energy, the longer the lifetime. Muons are typically produced at a height of 15 km, and lose about 2 GeV from ionization by interaction with air before reaching the surface of the Earth. The mean energy on ground level is $\approx$ 4 GeV [3]. The energy distribution varies with the angle.

2.2.7 Space weather influence on the muon flux

Satellite measurements show that the flux of galactic particles is depressed and their energy spectrum distorted by the Sun's proximity. This so-called solar modulation arises from the fact that the galactic particles which are continually diffusing into the inner part of the solar system are opposed by the solar magnetic fields carried outward by the plasma clouds. This effect is most pronounced in periods of enhanced sun spot activity [21]. The sun spot activity can spurn solar flares or even coronal mass ejections, which blast large amounts of

particles into the solar system. This can lead to a disruption in the Earth's magnetic field. As the galactic cosmic particles are influenced by this field, the flux of muons at ground level is also influenced.

Chapter 3

Detector Design

Muons that reach the Earth's surface can be detected in several ways. The CRT is a scintillation detector, which consists of four layers of scintillators. Each layer holds four scintillator-plates with area 25×100 cm^2, giving an active area of 100×100 cm^2 for each layer.[1] Two layers form a level, and the two layers of a level are perpendicular to each other. In this way, each level can be divided into 16 25×25 cm^2 pads when data from the two layers of a level are combined. This configuration allows a certain angular distribution to be measured. The two levels are separated by a flexible gap of $10-180$ cm. This gap can be adjusted by moving one or both levels up or down. In total, there are 16 scintillators, and therefore 16 read-out channels. The final readout is "yes - no", meaning that the detector only tells us if there was a hit in a scintillator or not. A sketch of the detector setup is given in figure 3.1.

3.1 Scintillators

A charged particle traversing a material can loose energy either through Cherenkov-radiation, transition radiation, bremsstrahlung or through an ionization process. In a scintillator, a traversing charged particle ionizes the scintillator material's active component(s). The ionized electrons will join an atom again, emitting one or several photons as they do so. Depending on the nature of the scintillating material, these photons have wavelengths in the visible or near-visible electromagnetic spectrum, specified by the energy levels of the atoms in the material. If the scintillation light is non-visible, a second component in the scintillator is used to shift it to visible light. This light signal is transported through the scintillator and read out. In order to transport light, the scintillator must be transparent. The processes creating the light signal is totally different in inorganic and organic scintillators.

The scintillators used in the CRT are organic scintillators. They consist of two fluorescent dyes, which are the active components, mixed into a polymer. Some technical specifications

[1] The scintillators have a thickness of 2 cm.

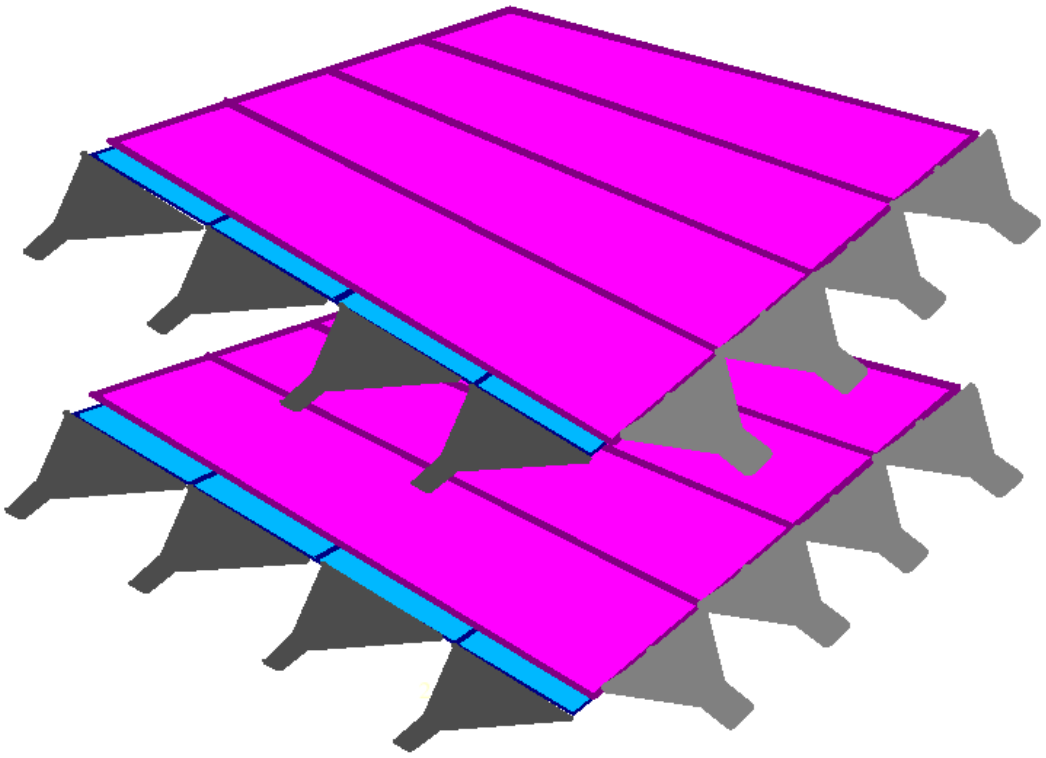

Figure 3.1: The purple and blue rectangles are scintillators, forming two layers. The gray triangular shapes at the ends are light guides. The purple and blue layers together form a level. There are two levels. Figure courtesy of Anna Lipniacka.

are listed in table 3.1. A charged particle traversing the scintillator excites the molecular levels of the primary fluorescent, and the time this takes is called the rise time. The exited states then decay, sending out UV photons, which gives the decay-time. Because of different excitation levels in the fluorescent, the decay-time has a fast and a slow component [22].

UV photons are absorbed in most transparent organic materials (i.e. the polymer), with an absorption length of a few millimeters. In order to get a signal, a second fluorescent dye is introduced. This absorbs the UV photons and emits them as photons in the optical range (acting as a wave length shifter), which are not absorbed by the polymer. Again, this process has a rise time and a decay time. The wave length shifter is chosen so that it's absorption spectrum matches the emission spectrum of the primary fluorescent. The spectrum of the emitted optical light typically ranges over about 100 nm, with a characteristic peak for different materials. The emission spectrum of the CRT scintillators is shown in figure 3.2. The light yield of the scintillator is a measure of how much of the initial ionization energy is converted to a readable light signal. The optical photons then traverse the scintillator, contained by multiple total reflections at the surface. The scintillators are also covered by aluminized mylar to contain prospective runaway photons. The mylar is then covered with black tape to make the scintillators as light-proof as possible. If light (i.e. photons) penetrate into the scintillator, they propagate through the scintillator in the same way as

Base (polymer)	Polyvinyl-toluene
Fluorescent dyes	N/A
Light yield, %Anthracene	64
Rise time, ns	0.9
Decay time (main component), ns	2.1
Wavelength of max.emission, nm	425
Refractive index	1.58
Density	1.032 g/cm^3

Table 3.1: Some properties of the plastic scintillators used in the CRT; St.Gobain BC-408

the light signal from the muons. A slight leakage of light onto the scintillators creates a much larger noise signal than muon signal. If the scintillators were not covered at all, it would create a continuous noise signal, and no information of the muons would be retrievable.

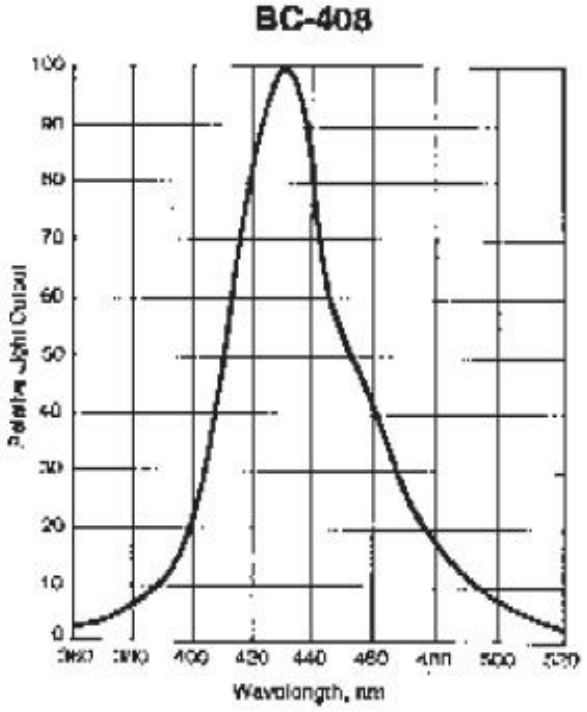

Figure 3.2: The relative light output of the CRT scintillators; St.Gobain BC-408

The light yield of the CRT scintillators are given as 64 % of the light yield of Anthracene. Anthracene has a light yield of 50 % of NaI. NaI has a light yield of $4 \cdot 10^4$ photons/MeV [22], measured for minimum ionizing particles (MIP). A MIP has $\beta\gamma \sim 4$. For the CRT scintillators, this gives a light yield of $1.28 \cdot 10^4$ photons/MeV. The energy loss via ionization

can be calculated via a numerical formula known as the Bethe-Bloch equation [22]:

$$-\frac{dE}{dx} = \left(\frac{4\pi r_e^2 m_e c^2 N_0 Z z^2}{A\beta^2}\right)\left(ln\left[\frac{2m_e c^2\beta^2}{(1-\beta^2)I}\right] - \beta^2\right) \tag{3.1}$$

where N_0 is Avogadro's number ($= 6.022 \cdot 10^{23}\text{mol}^{-1}$), Z and A are the atomic number and mass of the scintillator, ze and $v = \beta c$ are the charge and velocity of the muons, m_e is the electron mass, $r_e = 2.8$ fm (the classical electron radius) and I is the effective ionization potential. Using this formula for a MIP, we find that a muon traversing 1 cm of scintillator looses a minimum of ~ 2 MeV via ionization, producing at least 2000 photons.

Organic scintillators have several advantages. For our purpose, the most important is that they are very fast. Because they have two active components, their speed is dependent on both. The decay-time of both the primary and secondary fluorescents is just 2.1 ns, which means that a signal can be read out only a few nanoseconds after a muon has traversed the scintillator.

At the end of the scintillators, the scintillation photons are led into light guides. These are non-scintillating pieces of Plexiglas that cover the whole edge of the scintillator and then gradually get narrower.

3.2 Photomultiplier tubes

At the end of the light guides, a device to register photons is needed. This is normally some sort of photo-detector - a device that converts the photons from the scintillator into an electrical signal. The CRT uses photomultiplier tubes (PMTs).

A PMT is a glass vacuum tube containing a photo-cathode, several dynodes and an anode. Photons entering the PMT hit the photo-cathode. This can produce an electron due to the photoelectric effect. The quantum efficiency of a photo-cathode varies from 0.004 - 0.3, meaning that 0.4 - 30 % of all photons hitting the photocathode are converted to photoelectrons. In order to maximize the output, the photocathode is normally chosen so that it's ionization energy matches the maximum output of the scintillator. In the CRT, we had to make due with the PMTs we inherited.

The photo-electron is accelerated toward the first dynode because of a potential difference. The potential difference is delivered by a PMT-base connected to the PMT. The base is powered by a high voltage source (in our case a HV-card). Hitting the dynode, the photo-electron produces several secondary low energy electrons. These are accelerated toward the second dynode, where more electrons are produced. This process is repeated 10 times, creating an avalanche of electrons. The potential difference between the dynodes is of the order 100-200 V. When the electrons leave the last dynode, they hit the anode, which gives an electric signal. The signal is of the order 0.2-2 V, depending on the amplification and efficiency of the PMT. An example of a signal from a PMT is given in figure 3.3. We see

from the figure that the rise time of the PMT is in the nanosecond range, making it very fast. The decay time of the PMT is several microseconds. This is because the electrons in the avalanche have different energies. This gives the characteristic shape we see in the figure, with a steep peak at the beginning and a tail following it.

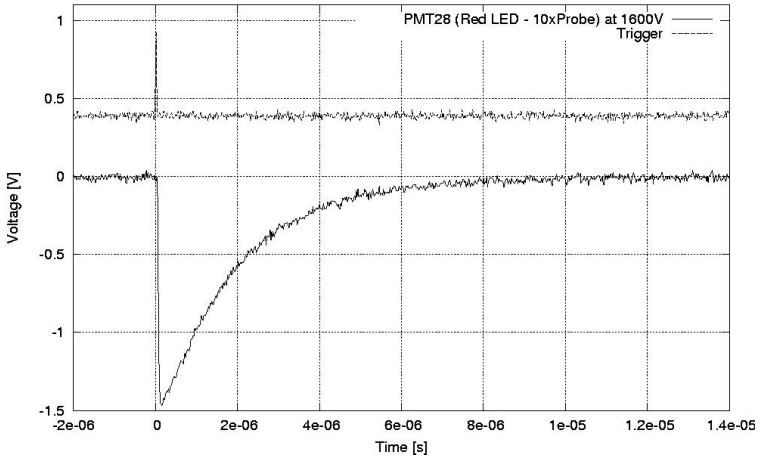

Figure 3.3: An analog signal from PMT 28. The signal was induced by a red LED probe at 1600 Volt

The PMTs are very sensitive to light. If there is light leakage onto the PMT, either onto the scintillator or directly onto the PMT, it will create a noise signal that is far greater than the signal originating from muons. In the CRT, the PMTs are mounted inside aluminum casings, both to ensure stability and to reduce light leakage.

3.3 Trigger cards

The trigger cards in the CRT receive an analog negative signal from a PMT as input. This signal is then run through a preamplifier and subsequent amplification, and is fed to an op-amp[2] with an adjustable and high amplification. The op-amp in effect operates in saturation, and the signal is fed to a monostable latch that gives a preset 200 ns, 5 V positive pulse when triggered. As seen in figure 3.3, the analog signal has a steep negative slope when the PM-tube is activated by a traversing muon. Therefore, the trigger cards send out a pulse <200 ns after the first electrons reach the anode of the PM-tube, with a variation among the trigger cards of ± 40 ns. The trigger cards were made and tested by Lars G. Johansen.

In the process of digitizing the signal from the PMT, all pulse height information from the initial muon contained in the analog pulse is lost. The trigger card sends the same signal

[2] operational amplifier

regardless of what energy the initial muon had. This is why we say that the CRT is a "yes-no" detector; it only tells us if there was a hit in a given channel or not.

3.4 Data read-out card with FPGA

The signals from each trigger card are sent to an FPGA[3] on the read-out card. All 16 trigger cards are connected in parallel to the FPGA. An FPGA is a programmable logic unit, allowing existing logical structures to be tailored to a specific operation by means of a hardware description language, such as VHDL in this case. The FPGA is run at 10 MHz, meaning that it has a time resolution of 100 ns, which gives the width of a time-bin. Every 100 ns the FPGA checks the input from the trigger cards to see if there is a signal. The threshold of the FPGA input is 1.7 V, meaning that the FPGA reacts if one of the channels gives a signal with a height of at least 1.7 V. The upper threshold is 4.0 V.

If there is a signal from at least one of the trigger cards, the FPGA reads out all 16 channels. Since the signals from the trigger cards are 200 ns, a hit is almost always recorded twice, in two adjoining time bins. This overlap is implemented to avoid loss of any signals, and must be considered in the analysis [4]. A hit is denoted as 1, while no hit is denoted 0 in the data file. A graphical interpretation of the signal from the trigger card and readout from the FPGA is given in figure 3.4.

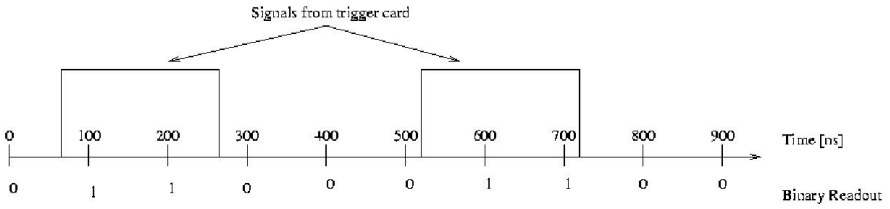

Figure 3.4: Trigger readout. The rectangles are asynchronous digital signals created by the trigger cards; 200 ns long and 5 V high. The time-line shows the time-bins of the FPGA's clock. At the start of each time-bin, the signals from each trigger card are checked. If there is a signal on one channel, it is denoted by a "1", if not it is recorded as a "0", i.e. "binary readout".

16 channels give 16 bits of data. These are sent to a FIFO ("first in first out") structure along with a 30 bit time-stamp and two control bits. The time-stamp comes from the time-bin the signals are recorded in. The size of the time-stamp limits a cycle of the internal clock to $2^{30} \cdot 100$ ns, which is approximately 107 seconds. After this time, the time-stamp starts over at zero. The first control bit is a calibration bit that is set to "1" if a calibration

[3] Field-Programmable Gate Array

[4] A signal from the trigger card that starts at the same time as a time-bin starts, creates a metastable state that can be read out as either a signal or not. By using a 200 ns signal from the trigger card, the probability of metastability is virtually non-existing.

trigger is sent to the FPGA from the computer software. The second control bit is set to "1" if the FIFO readout is cleared using computer software. The FPGA on the read-out card was programmed by Magne Munkejord. A schematic overview of the FPGA program for the CRT is given in figure 3.5.

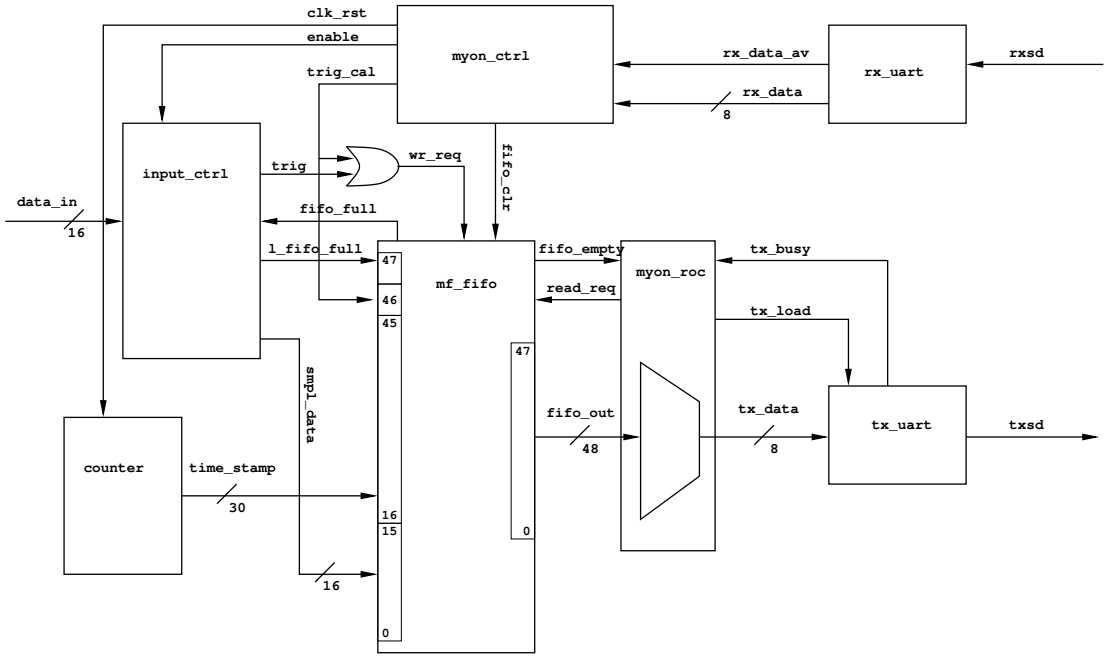

Figure 3.5: A schematic overview of the FPGA structure [23]. Data from the 16 trigger cards are read by an input control and transfered to a FIFO together with two control bits and a 30 bit time-stamp from the clock. The FIFO then sends the 48 bit string to the readout controller which is a 48-in, 8-out multiplexer which connects to the FPGA I/O.

The 48 bit string (containing signal data, time-stamp and control bits) is sent from the FPGA's embedded RS232 controller to an external USB converter on the read-out card. The converter then connects to a computer's USB connection. Each string is written as a line in a data-file using a readout program in LabVIEW [5]. The 16 bit from the trigger cards are written with channel 1 to the right and channel 16 to the left. The time-stamp is written as a regular number, not a binary number. An example of the file format is given in table 5.2. Real-time monitoring is provided for by the readout software (i.e. LabVIEW), while analysis of the data-file is carried out off-line using ROOT. The analysis program is described in detail in chapter 5.

3.5 Power supplies

In order to run smoothly, the detector requires a stable power supply. Both the PMTs and the read-out electronics have to be powered.

[5] The readout program was made by Lars G. Johansen

The PMTs are powered by HV-cards. Each card consists of a HV-source (EMCO CA20N-5), a potentiometer, a capacitor and input-output pins. The HV-cards are powered by 4 computer power supplies (Chieftec SI-A300P3), one for each layer, that deliver 5 V. The HV-source converts a 5 V input to a 0-2000 V output [6]. The output is regulated by the potentiometer. The HV-source also provides a reference voltage of 0-2.048 V, which corresponds to the HV output. In this way, it is possible to monitor the HV output without measuring it directly.

The trigger cards need two different voltage inputs. The analog amplifier requires 24 V, whereas the digital part runs on a 5 V supply. Both of these are delivered by a laboratory power supply (TTi EL302 Tv). Because the currents involved are so low, one power supply is sufficient for all 16 trigger cards. The FPGA runs on a separate 5 V supply (Powerbox 3000).

[6] To function properly the input must be between 4.75-5.25 V

Chapter 4

Construction and Testing of the CRT

A large part of the work in this thesis was producing the various components and parts needed to make the detector work, and assembling them in the final detector setup. Various testing procedures were also carried out.

4.1 Framework

The active components in the CRT are the scintillators and readout electronics described in chapter 3. To ensure that these components are kept as stable and aligned as possible, they were placed in a framework made of aluminum girders. 5 girders were bolted vertically to the floor using concrete bolts. In addition, two of the girders were bolted to the walls via steel brackets. Two horizontal frames were placed inside the vertical girders. The frames were made by connecting aluminum girders with screws and links. This method of joining the girders gives more flexibility than welding the pieces together.

The scintillators were placed on rails attached to the frames and were not fastened in any way. At the light guide end of the scintillators, the frames have room for the PMTs. The PMTs were placed inside aluminum holders. These holders were screwed onto brackets on the frames. There is no glue or similar substances between the light guides and the PMTs; they are simply pressed together. A picture of the framework is given in figure 4.1.

4.2 Scintillator wrapping and light guide assembly

As described in chapter 3, the scintillators and light guides are wrapped in mylar. Mylar is a trade name for biaxially-oriented polyethylene terephthalate (boPET) polyester film [24]. The mylar we used is aluminized on one side, making it a very good reflecting material. The wrapping process was carried out in several stages in a clean room. First, the scintillators and light guides were cleaned using ethanol and wrapped in mylar. The mylar was then covered in black electrical tape. The tape was used both for keeping the mylar in place

Figure 4.1: The framework of the CRT before mounting the active components.

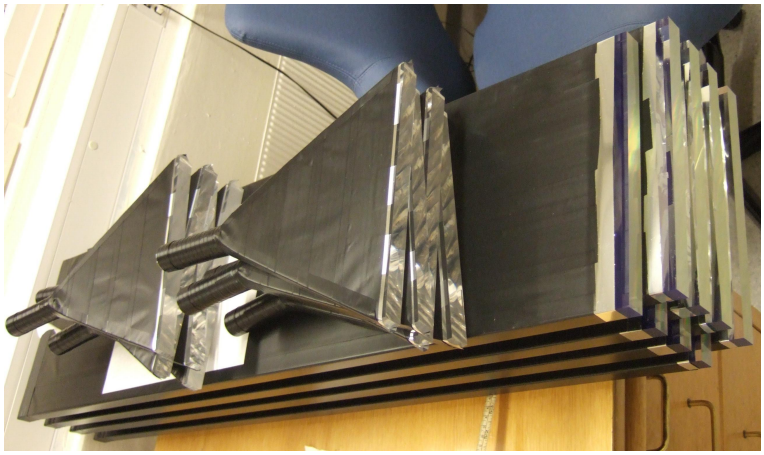

Figure 4.2: 8 scintillators and light guides wrapped in mylar and electrical tape, ready to be glued together.

and for making the scintillators and light guides as light-proof as possible. A picture of wrapped scintillators and light guides is shown in figure 4.2.

The scintillators and light guides were joined with optical cement. To ensure a minimal loss of light signal, the optical cement has a refractive index that matches the refractive index of the scintillators. It consists of two parts; resin and hardener. Approximately 28 parts hardener was added to 100 parts of resin. This mix was then placed in a vacuum chamber to extract all air bubbles from the mixture. As the pressure drops, air expands many times in volume, while the optical cement mixture stays approximately the same. The result is that the air bubbles burst as they grow bigger, relieving the mixture of air bubbles. The process is called "vacuum cooking". If this had been omitted, the microscopic air bubbles would have deteriorated the transparency of the optical cement. When the mixture was ready, a thin layer was placed on the end of the scintillators and the light guides were pressed onto it. They were left to dry for about 24 hours before the remaining gap between scintillator and light guide was covered with mylar and tape.

4.3 Production of HV-cards for the PM-tubes

The HV-cards for the PMTs were produced in several steps. First, a schematic layout was drawn using Eagle. This is shown in figure 4.3. The pattern shows where the card is intended to have electrical circuits. The schematic drawing of the card was printed onto a plastic transparency, with the circuits in black. The transparency was fastened to a circuit board. A circuit board is a piece of non-conducting material (substrate) laminated with a layer of copper. The copper is covered with a UV-sensitive, acid-proof film. The circuit board with the transparency was placed under UV-light for about one minute. This is called "developing", and deteriorates the film in all areas where it is not covered by black circuit lines on the transparency. After the developing, the transparency was removed, and the card was placed in an acid bath. The acid etches the copper where the film is deteriorated, leaving copper circuits where the print on the transparency was. The remaining film was then washed off. The copper circuits were then covered in tin to make the soldering process easier.

The components of the HV-card were then soldered onto the card.

4.4 Efficiency testing of PMTs

The PMTs and PMT-bases for the CRT where inherited from an old project at CERN. To determine their efficiency and if they functioned adequately, we did an efficiency test.

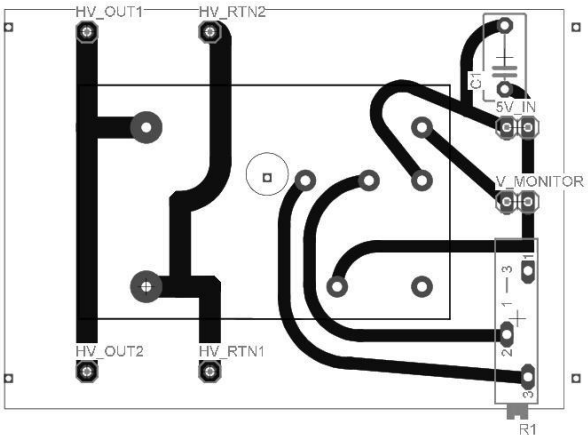

Figure 4.3: A schematic drawing of the circuit board layout for the HV-cards.

4.4.1 Test setup

Three scintillators with light guides were placed on top of each other at a distance of ≈ 5 cm. The light guides were then inserted into a box. The box was covered in tape to make it as light-proof as possible. We then chose two PMTs at random to be reference tubes, # 10 and # 26 [1]. These were attached to the upper and lower scintillators inside the box and held at 1800 V. We then attached all the other PMTs in turn to the scintillator in the middle, and counted double and triple coincidences with the middle tube at different voltages. The HV-sources for the final setup were used. A double coincidence was defined as a hit in the upper and lower scintillators with a time difference of less than 100 ns. Similarly, a triple coincidence was a hit in all three scintillators with a time difference of less than 100 ns. A picture of the setup is shown in figure 4.4.

In order to get applicable signals, we used the trigger cards from the final setup (described in chapter 3) to convert the analog signals from the PMTs to digital signals. The digital signals were then transfered to a circuit containing a NAND chip and a monostable latch. This circuit gave two outputs; a 100 ns signal for each double and each triple coincidence respectively. The number of double and triple coincidences was registered manually using two counters. Each PMT was tested for 1-3 minutes at several voltages ranging from 1500-1900 V. A count of the total number of signals from the test tube at 1900 V was also registered. All signals in the test tube that were not associated with a triple coincidence, were considered as noise. By noise we mean a count that is not induced by a muon. Noise can originate from photons entering the scintillator/PMT, or the PMTs creating electrical signals.

[1] All the PMTs had numbers from the former project. We used this numbering to distinguish between them.

Figure 4.4: Efficiency test set-up: Three scintillators on top of each other with PMTs inside a light-proof box.

4.4.2 Statistical errors and efficiency

In the test set-up, we compared the triple coincidence rate of all three tubes with the double coincidence rate of the reference tubes. We assumed that the probability of getting a triple coincidence when we had a double coincidence, was given as a binomial distribution with probability p. We found p by dividing the number of triple coincidences N_3 by the number of double coincidences N_2 in a given interval. We defined this ratio as the efficiency ϵ of the PMT:

$$\epsilon = p = \frac{N_3}{N_2} \tag{4.1}$$

The variance of a binomial distribution is given as:

$$\sigma^2 = np(1-p) \tag{4.2}$$

where n is the number of times the test is repeated. In our case, $n = N_2$. The variance of the triple coincidence rate was then:

$$(\Delta N_3)^2 = N_2 \frac{N_3}{N_2}\left(1 - \frac{N_3}{N_2}\right) \Longrightarrow \Delta N_3 = \sqrt{N_3\left(1 - \frac{N_3}{N_2}\right)} \tag{4.3}$$

The error $\Delta\epsilon$ and relative error $\frac{\Delta\epsilon}{\epsilon}$ in the efficiency ϵ was given as:

$$\begin{aligned} \Delta\epsilon &= \frac{\Delta N_3}{N_2} = \frac{\sqrt{N_3\left(1 - \frac{N_3}{N_2}\right)}}{N_2} \\ \frac{\Delta\epsilon}{\epsilon} &= \sqrt{\frac{1}{N_3} - \frac{1}{N_2}} \end{aligned} \tag{4.4}$$

In this test, $\frac{\Delta\epsilon}{\epsilon} < 2\%$ was considered acceptable.

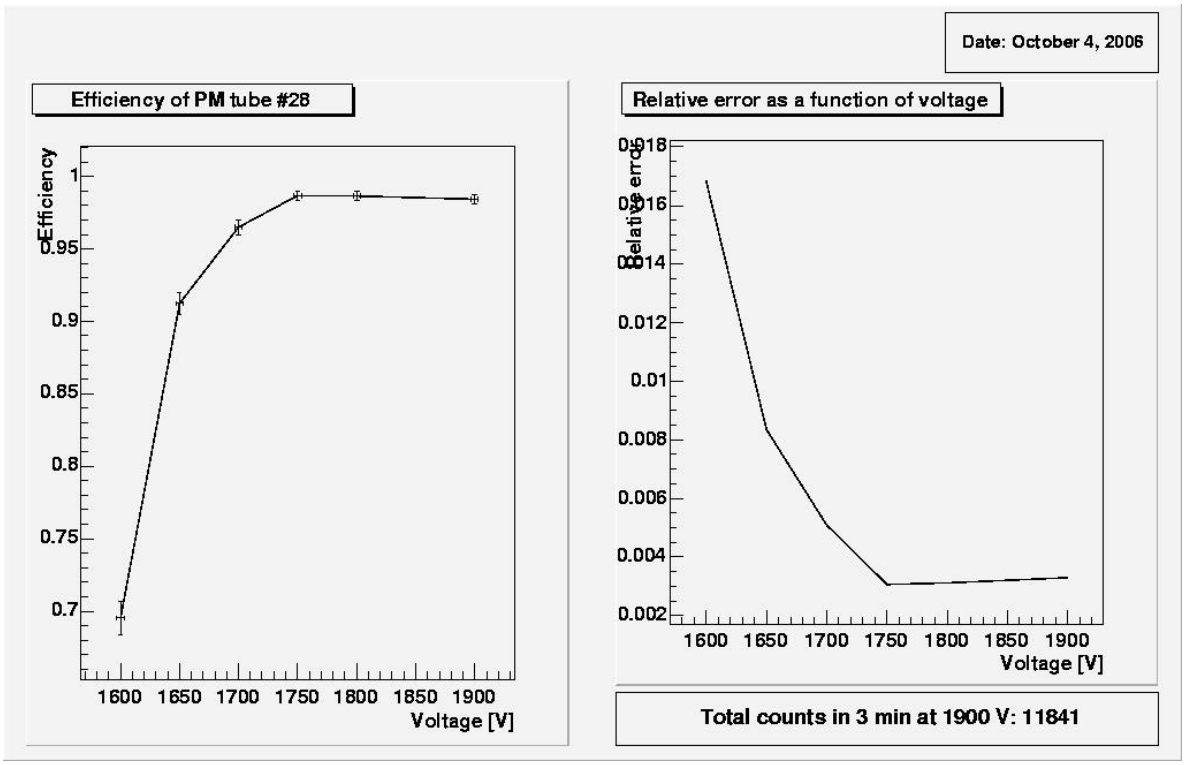

Figure 4.5: Efficiency and relative error plot for PMT # 28

4.4.3 Test results

We had a total of 20 PMTs. 17 were tested with #10 and #26 as reference tubes. The last three[2] were tested with #27 and #30 as references. The behavior of most of the tubes was similar, and an example of an efficiency plot is given in figure 4.5. The efficiencies of the PMTs are summarized in table 4.1, listing the lowest voltage that surpassed an efficiency of 95 %.

During the efficiency testing, we experienced a varying degree of noise in the different PMTs. The most sensitive PMTs had a noise-to-signal ratio of 10-100 at 1900 V. In the test setup, this had negligible significance. If this ratio persisted in the final setup, it would demand a reprogramming of the FPGA. To explore the nature of the noise, we first blinded the two reference PMTs. The result was that they did not give any signal. This implied that the noise was not of an electrical nature.[3] We continued our search for the noise source by attaching PMTs #10 and #30 to two scintillators [4], and tuning the voltage to 1700 V. The double coincidence rate and total rates of #10 and #30 were registered as before without any cover on the scintillators. #10 had a signal frequency of 400-800 Hz, while

[2] #10 and #26 in addition to #22

[3] The completion of the detector described below showed that most of the PMTs indeed had electrical noise. This would have been detected if we had blinded all the PMTs instead of just two.

[4] According to the testing, these PMTs were the most efficient.

PMT #	Efficiency [%]	at Voltage [V]
11	The efficiency is always below 95 %	-
38	97.5379	1900
28	96.4975	1700
48	98.4257	1900
06	98.6572	1900
45	98.1039	1900
27	98.8674	1600
30	97.6718	1650
40	97.6266	1900
07	95.4447	1900
46	98.5485	1750
16	97.9926	1700
43	98.2759	1850
42	99.8201	1800
41	96.7132	1800
18	97.3154	1800
19	97.3984	1700
26	The efficiency is always below 95 %	-
10	95.0427	1600
22	98.5267	1600

Table 4.1: The efficiencies of the PMTs with the lowest voltage exceeding 95 % efficiency.

	Total rate [Hz]	Noise-to-signal ratio
Double coincidence	19.9	1.0
#10	55.0	2.8
#30	39.8	2.0

Table 4.2: Total and double coincidence rate after covering the test setup with light-proof material.

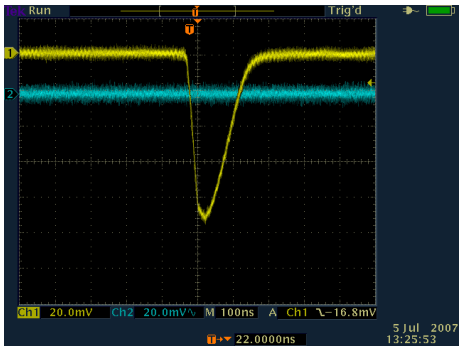

Figure 4.6: Analog test signal (yellow) used for testing and calibrating the trigger cards of the CRT.

#30 had 40-50 Hz. The double coincidence frequency was 20-30 Hz [5]. The whole setup was then covered with a double layer of light-proof material and the test was repeated. The results are given in table 4.2. They show that covering the setup reduced the noise, confirming that there was light leakage in the scintillators or light guides. Because of this, the final setup was enclosed by a tent of light-proof PVC.

4.5 Calibration of trigger cards and testing of signal cables

The trigger cards were connected one by one to a signal generator for testing and calibration. The signal from the generator was set to resemble the real analog signal from the PMTs, with a negative peak of 90 mV and a length of approximately 150 ns. The peak is assumed to have the minimum height that a real signal can have, meaning the most real analog signals from the PMTs will have a higher peak. The length of the signal is considerably shorter than for a real signal, but since the cards trigger on the inverted positive slope, this does not matter. A picture of the test-signal, as viewed on an oscilloscope, is shown in figure 4.6.

The amplification on the trigger card can be regulated by two potentiometers. The first regulates the sensitivity of the preamplifier. We regulated all these first potentiometers so that the cards had a maximum sensitivity to the analog signal without distorting it. The second potentiometer regulates the sensitivity of the digital stage by adjusting the feedback resistor of the op-amp that connects to it's input. Below a certain level, the digital signal

[5] Because of the large variations in #10's frequency, only an order of magnitude measurement was taken.

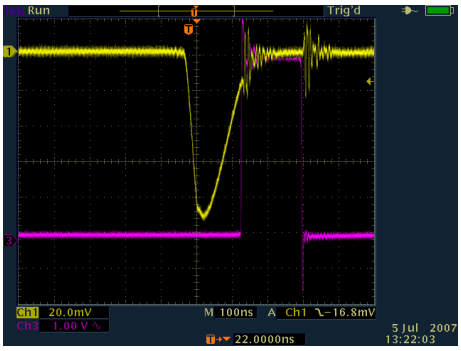

Figure 4.7: Digital signal from a trigger card (purple) together with the analog test signal. Notice that digital noise from the output is seen on the test signal. We also see that the digital signal is sent from the trigger card approximately 150 ns after the start of the analog signal.

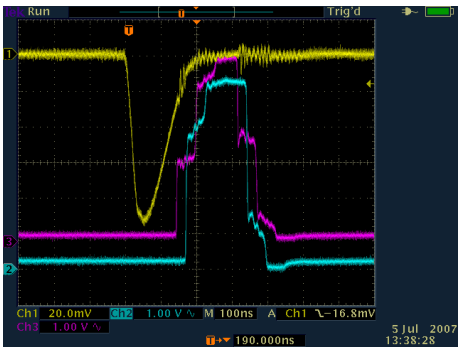

Figure 4.8: A digital signal from a trigger card recorded at the two ends of a coaxial cable. We see that the signal both as it exits the trigger card (purple) and at the end of the cable (blue) is distorted. Notice also the time difference between the two signals. This shows that the signal propagates through the cable in approximately 25 ns.

is lost, and the second potentiometer was adjusted to this level in order to have an equal trigger-level for all readout cards. Figure 4.7 shows the digital output together with the test signal.

In the detector, the digital output from the trigger cards is sent to an FPGA on the readout card. The signal is carried by a coaxial cable to avoid loss or disturbance from other electromagnetic sources, such as power cables and other channels. The problem with a long cable is that the digital signal is reflected at the receiving end, distorting the signal. This is shown in figure 4.8.

The problem of reflection of the signal was remedied by introducing a resistance in parallel with the signal cable at the receiving end. In addition to reducing the distortion of the signal, the resistance also reduced the height of the signal. As mentioned in chapter 3, the signal height from a trigger card is 5 V, while the maximum voltage allowed into the FPGA is 4.0 V. The value for the resistance was found by adjusting a potentiometer to optimize the shape of the signal, and was set to 150 Ω. A capacitor was installed in series with the

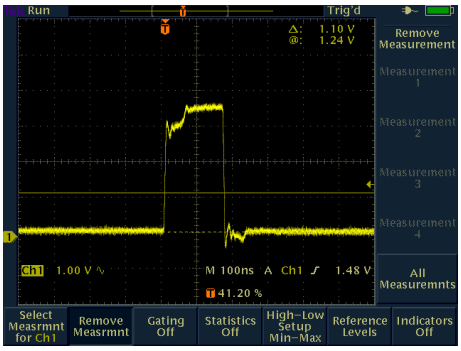

Figure 4.9: A muon (or noise) signal after passing through the impedance card. Notice that the signal is still misshaped. This is of no importance as long as it is above 1.7 V and below 4.0 V.

readout to cancel any voltage-level difference between the trigger card and readout card. When coupling a capacitor to such a circuit, it reduces the signal gradually. By choosing a large enough capacitor (100 nF), this reduction has a much higher time constant than the signal pulse. The capacitors and resistances were soldered to an impedance card. This was connected to the read-out card. An example of a signal read out at the impedance card is given in figure 4.9. This signal was taken using a scintillator and belonging electronics.

4.6 CRT control unit

In order to have control over the power to the components of the detector, we found it necessary to fabricate a control unit. The unit is essentially an aluminum box divided into three sections. In the upper part, all wires powering the trigger cards are connected to wires from the laboratory power supply. In the middle part, all the signal cables from the trigger cards are soldered to the impedance card, which in turn is connected to the read-out card. A USB wire connects the read-out card to a computer. The lower part consists of a panel of buttons. Four of the buttons control the computer power supplies. In addition, each HV-card has it's own designated button. This is done both for safety reasons, as well as to allow separate channels to be run individually without having to detach wires. A picture of the CRT control unit is shown in figure 4.10.

4.7 Testing and debugging of the final setup

Before the light-proof tent was finalized, a thorough test of all the channels (i.e. readout from each trigger card connected to a scintillator and PMT) was carried out.

4.7.1 First single channel testing

When all the PMTs, trigger cards and HV-cards were mounted and soldered together, a test of all the channels was conducted. Each channel was tested separately, using the

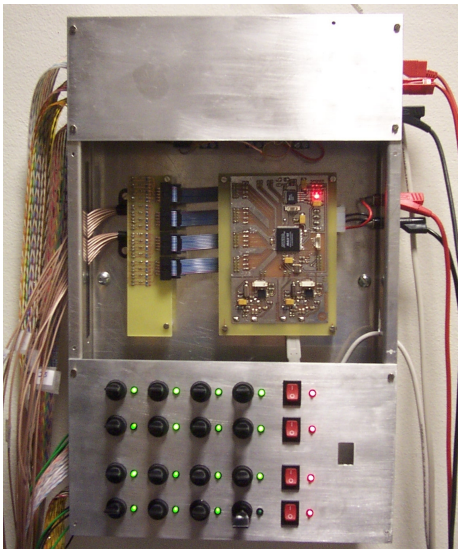

Figure 4.10: CRT control unit.

laboratory power supply (TTi EL302 Tv) to power both the HV-card and trigger card. The PMT's voltages were chosen using table 4.1. The readout from the trigger card was registered using a universal frequency counter (TTi TF830). To minimize light leakage, the PMTs were covered in light-proof cloth. This did not remove the light leakage, but reduced it sufficiently to avoid an overload of the PMTs. The results of these first single channel tests are given in table 4.3.

The single channel testing revealed several important faults. First, it was clear that the long cables supplying the HV-cards resulted in a considerable drop in the voltage at the HV-cards. The HV-sources demand a voltage between 4.75-5.25 V as input to function properly. In the test, this was compensated by turning up the voltage on the laboratory power supply. In the final setup, the computer power supplies powering the HV-cards were mounted directly onto the framework close to the HV-cards, thus avoiding long wires and a voltage drop.

Secondly, only 9 out of 16 channels functioned as they should. Looking at the test results in table 4.3, it seemed as if two different faults were occurring. PMT 38 and 43 simply did not give any signal, while PMT 19 had a very low rate. PMTs 46, 40 and 28 were partly functioning, but it was clear that something was wrong. We measured a considerable voltage difference (ranging from 100 V to over 1000 V) between the frame and reference voltage output, HV-source casing and the capacitor on the HV-card, and also observed sparks between the monitor output and the frame when measuring this voltage for PMT 40. Spark noises were heard inside the aluminum casing of both PMT 46 and 40. This could indicate a short circuit of some sort.

PMT #	HV-value [V]	Volt. in [V]	Volt. PS [V]	counts 1 min	Status
18	1850	4.93	6.3	35500	ok
45	1900	4.93	6.4	21000	ok
41	1800	4.98	6.2	1-8 kHz	ok
40	-	-	-	-	possible short circuit
28	1750	5.05	6.0	5400	possible short circuit
30	1700	4.80	5.9	7400	ok
27	1650	4.88	5.9	19900	ok
19	1750	5.01	6.0	<1 Hz	virtually no signal
48	1900	4.86	6.1	5800	ok
42	1800	5.06	6.1	19500	ok
38	-	-	-	-	no signal
43	-	-	-	-	no signal
16	1750	5.04	6.0	24000	ok
22	1600	4.96	5.8	7500	ok
46	-	-	-	-	possible short circuit
10	1650	5.05	5.9	8000	ok

Table 4.3: First results from single channel testing. "Volt. in" gives the voltage that the HV-source (EMCO CA20N-5) receives. "Volt. PS" gives the voltage that the power supply must deliver in order to produce the "Volt. in" at the HV-card. The difference in the two is due to a voltage drop because of resistance in the long wires supplying the HV-card. We see that some of the channels have faults.

4.7.2 Debugging the possible short circuits

The first thing we checked, was if the HV-sources were the cause of the malfunction. The HV-source of PM-tube 40 was detached from the setup, and we tested it separately. It functioned properly. We then interchanged the HV-cards of PMTs 10 and 46 and turned them on separately. The result was that PMT 10 still worked, while 46 did not. We concluded that the HV-sources were not the cause of the malfunction.

After ruling out the HV-sources, we turned our attention to the PMTs and their bases. Because of the voltage measured on the frame and HV-card reference voltage, we suspected that the aluminum casing surrounding the PMTs might be causing the problem. We therefore removed PMT 46 from the frame and blinded it inside a light-proof cloth. It still malfunctioned, and we read a voltage of $\sim$ 280 V from the reference voltage, HV-source casing and capacitor to the frame. We tried removing the aluminum casing, and had similar results. This led to the conclusion that the aluminum casing was not responsible for the malfunction.

PMT 46 was still not working properly after we removed it from the aluminum casing. To see if we could locate the areas where the sparks were coming from, we mounted it once again on the frame and attached it to a scintillator. We turned on the HV-card and started at a low voltage. At first, nothing happened. We gradually increased the voltage. Exceeding 1800 V, we observed sparks in several places on the base, and the PMT malfunctioned. The sparks came in irregular intervals.

On closer inspection, we discovered that several of the components on the base were charred at the legs connecting them to the circuit board. A further inspection revealed that this coincided with a poor soldering on one or both of the legs of the component[6]. In addition, we also discovered that one of the resistances, a 1.1 kΩ resistance sitting at the input end of the base, also had a charred body and looked as if it had been overloaded.

As a solution to the problems described above, we re-soldered all the components on the base of PMT 46. We also replaced the 1.1 kΩ resistance that had been overloaded. The new resistance was chosen with a higher power acceptance [7]. We re-mounted PMT 46 and turned it on at 1850 V. After a 30 minute run, where the measured rate was in the kHz area, we concluded that the PMT now functioned properly. Because the poor soldering could be a problem sooner or later also for the PMTs that functioned in the first single channel testing, we decided to re-solder all the components and replace the 1.1 kΩ resistance on all the remaining bases. When this was done, we connected all the PMTs to the scintillators and tested all the channels again.

---

[6] The PMT-bases are double-sided, having conducting pathways on both sides. The components can then be soldered on both sides. Apparently, some of the components were only soldered on the backside, creating an unstable connection on the front-side.

[7] Apparently, the 1.1 kΩ resistance originally placed on the base was overloaded because the current running through it was too high. We therefore replaced it with a resistance that could handle twice the power.

PMT #	HV-value [V]	Volt. in [V]	counts 1 min	Status
18	1850	5.04	37500	ok
45	1900	5.03	51000	ok
41	1800	5.06	242000	ok
40	1900	5.02	48000	ok
28	1750	5.07	20900	ok
30	1700	5.08	43500	ok
27	1650	5.08	29500	ok
19	1700	5.08	47000	ok
48	1900	5.03	13300	ok
42	1800	5.05	4800	ok
38	1900	5.04	13800	ok
43	1850	5.04	58000	ok
16	1750	5.05	91000	ok
22	1600	5.06	15000	ok
46	1750	5.05	218000	ok
10	1650	5.05	42500	ok

Table 4.4: Results from second single channel testing. "Volt.in" is still the voltage that the HV-card receives from the power supply (computer power supply). The number of counts in 1 min varies hugely due to the random covering of each PMT and variations in PMT efficiencies. The frequency is much higher than expected in the final setup.

4.7.3 Second single channel testing

For the second single channel testing, we used the computer power supplies (Chieftec SI-A300P3)[8] to power the HV-cards instead of the laboratory power supply. The power supplies were mounted on the frame of the detector to avoid long wires and the voltage drop we experienced in the first single channel testing. In addition, a relay was coupled to the HV-in, so that each HV-card could be turned on and off individually using the buttons in the CRT control unit. Each PMT and corresponding light guide was covered with light-proof cloth. The results of the second single channel testing are given in table 4.4.

The second single channel testing showed that all 16 channels were giving signals and did not malfunction. We therefore proceeded by putting the PMTs into their aluminum casings. These were then connected to the light guides and fastened to the frame. All wires were connected in the control unit described above, and the FPGA was connected to a computer.

[8] The computer power supplies demand a certain load to function. Resistances were therefore coupled to each of the voltages on the supplies to ensure that they functioned.

4.7.4 Third single channel testing

Before finishing the light-proof tent, we wanted to perform one last single channel test. We used the FPGA to read out data from each channel, while covering the tested channel as before. Unfortunately, on initiating this test, a mis-wiring of the trigger card power cables led to several of the trigger cards malfunctioning. This in turn led to a new debugging, this time of the trigger cards in question. Channel 13 had unresolved faults that we did not manage to locate due to lack of time. We proceeded with constructing the light-proof tent, and postponed debugging the last channel.

4.8 Light-proof tent

The various tests performed involving PMTs showed that the scintillators and connection between light guide and PMT are not light-proof. To ensure a completely light-proof setup, we built a tent of PVC material around the detector. The PVC material was fastened to a framework of wooden beams. At the ground, it was fastened with bolts. A hole in one of the beams was used for running cabling to and from the detector. Along the roof and wall borders, additional pieces of PVC overlapping the tent were fastened to ensure that the intersection did not let in light.

In order to have access to the detector, an opening was made in the PVC material. When running the detector, this opening is covered by an overlapping piece of PVC material that is held into place by neodyne magnets. The magnets are placed inside thin, aluminum rods, in order to have even closure of the slits instead of point-wise at the magnets.

With the tent finished, we initiated data-taking. Despite the tent, we still had a much higher rate in each channel than anticipated. A close inspection of the inside of the tent revealed that, despite being completely dark inside, we still had some light leakage at the borders. We tried mending this by shoving black felt into the cracks, but without success. As a final attempt at getting the tent light-proof and the rates down, we filled all the borders between the tent and the walls with black silicone. The silicone removed the last small cracks of light leakage, but still the rates for many of the channels were ranging from 200-1000 Hz, many times the expected muon rate. Since the tent now was light-proof, we concluded that the source of the noise was not light leakage. As a result of this, we were forced to make adjustments to the setup.

4.9 Voltage adjustments

Prior to the light-proof tent being installed, we had assumed that the noise was due to light leakage. This assumption was based on blinding the two reference tubes in the efficiency testing of the PMTs described above. Completion of the tent showed that the noise was in fact electrical noise from the PMTs. The noise was reduced by turning down the voltage

PMT #	HV-control voltage [V]	Rate [Hz]	Status
18	1.758	39	stable
45	1.650	32	stable
41	1.377	58	unstable
40	1.555	46	stable
28	1.692	42	stable
30	1.672	43	stable
27	1.487	42	stable
19	1.792	3	stable
48	1.581	39	unstable
42	1.447	47	stable
38	1.801	37	stable
43	1.676	48	stable
16	-	-	-
22	1.396	40	unstable
46	1.629	17	unstable
10	1.568	45	stable

Table 4.5: The PMT HV-values and rates after adjusting the voltage to acceptable rates. The status of each channel is also given.

on the PMTs until we had a single channel rate between 20 and 70 Hz. On doing so, we experienced that some of the channels were unstable and could suddenly increase their rate tenfold or more despite a drop in the voltage. Both the large noise rate and the instability of some of the PMTs can be a result of running them on higher voltages than they were fabricated for. We do not know if this instability is a fault in the PMTs themselves or the bases. A summary of the voltages and the approximate rate of each PMT is given in table 4.5. The rates were registered using a universal frequency counter.

The voltage adjustments concluded the construction of the CRT. Pictures of the finalized detector are shown in figure 4.11.

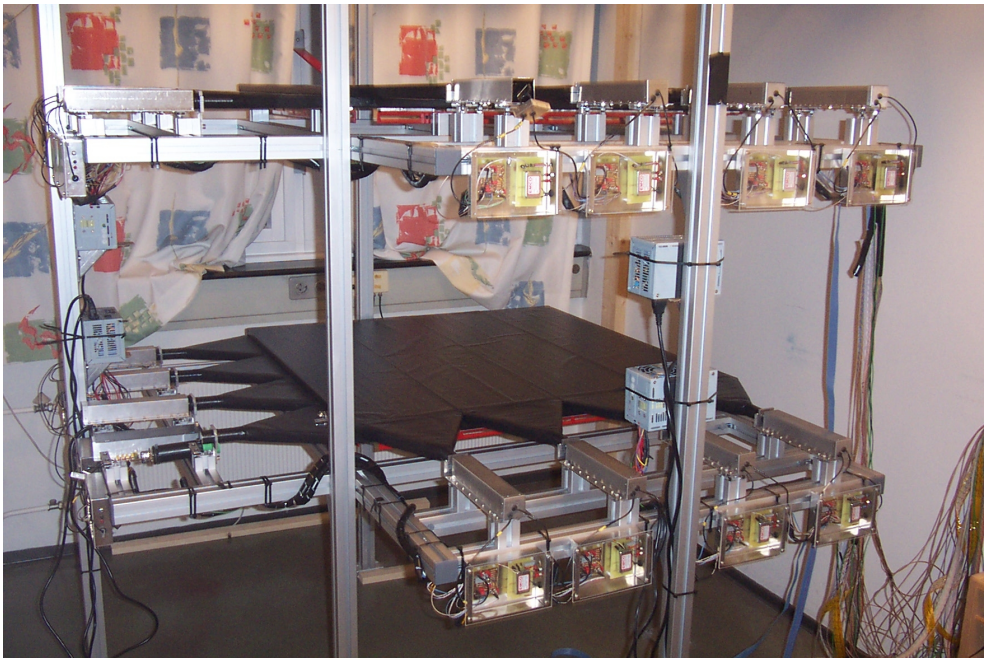

(a) The CRT before the construction of the light-proof tent

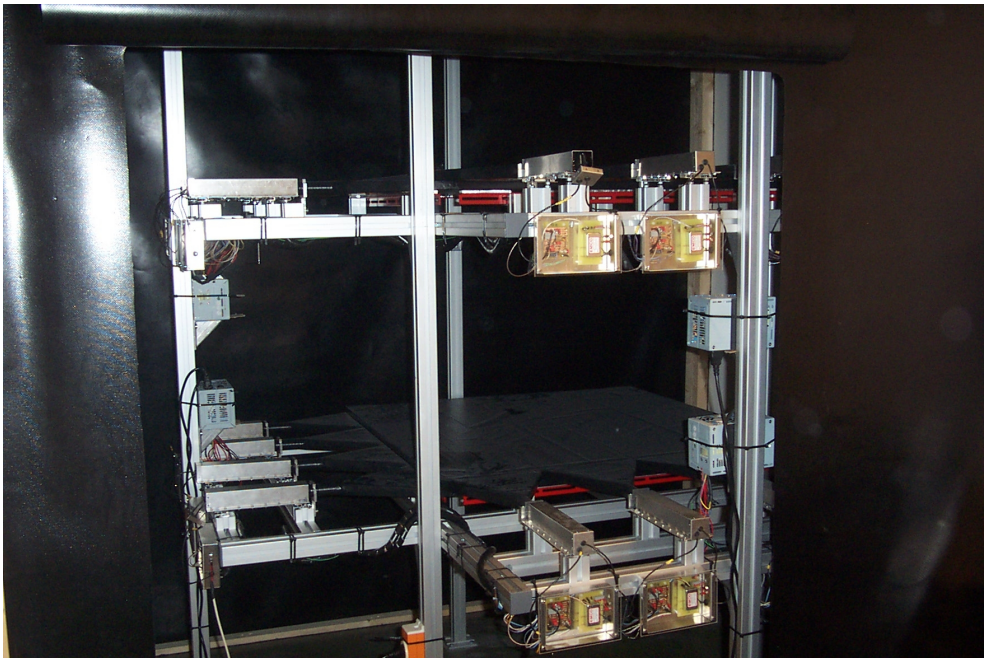

(b) The finalized CRT with light-proof tent

Figure 4.11: The CRT.

Chapter 5

Data Simulation and Analysis Program

The data from the CRT are written to file and analyzed off-line. In order to develop and test the analysis program for the CRT, we simulated data-taking and wrote the results to files with the same structure as the real data files. First and foremost, the simulations were performed because the development of the analysis tools needed data files that resembled those of the real data-taking. In addition, it is useful to compare the analysis of simulated data and real data. The simulation programs and analysis programs were written as ROOT macros.

5.1 ROOT

ROOT is an object-oriented software package developed by CERN. It was originally designed for particle physics data analysis and contains several features specific to this field, but it is also commonly used in other applications such as astronomy and data mining [25]. It has a variety of predefined classes and variables, such as histograms, graphs, random generators and so on. In this way, it can be used both for simulations and analysis. ROOT is run as a command line program that takes arguments in the C++ programming language. The syntax is therefore the same as for C++. It is also possible to compile macros in ROOT. In addition, ROOT allows incorporation of user defined classes and objects.

5.2 CRTGeometry class

The CRTGeometry class is a class that defines the entire geometry of the detector. All variables like scintillator length and width, distance between the levels and so on are stored here. Methods for setting and getting these variables are implemented, as well as several methods for calculating channel hits from coordinates or coordinates from channel hits.

The CRTGeometry class defines a coordinate system for the detector. The origin (0,0,0) is defined to be in the forward left corner of the lowest level (the corner where the light

Channel #	PMT #
1	18
2	45
3	41
4	40
5	28
6	30
7	27
8	19
9	48
10	42
11	38
12	43
13	16
14	22
15	46
16	10

Table 5.1: The PMT numbers corresponding to the channels defined using the CRTGeometry class.

guides of two and two layers in fig 3.1 meet). The x-axis is positive along the light guides of the upper layer, the y-axis along the light guides of the lower layer. The detector thus stretches from x/y = 0 cm to x/y = 100 cm. The z-axis is positive from the origin and upward to the first level, giving the first level a non-zero, positive z-coordinate of variable size (since the distance between the two levels is flexible). The upper level is defined as level 1, the lower as level 2. The numbering of the readout channels follow from the coordinate system. Channels 1-8 are in level 1, 1-4 following the x-axis and 5-8 following the y-axis. Channels 9-16 are in level 2, 9-12 following the x-axis and 13-16 following the y-axis. The corresponding PMT numbers are given in table 5.1.

5.3 CRTSimulation Macro

In the simulation of muon events, some basic parameters were used:

- The total flux (intensity) of muons in a horizontal detector is $I \approx 1$ cm^{-2}min^{-1} [3], leading to an approximate mean flux of 167 m^{-2}s^{-1} for the CRT. The total muon flux includes parallel muons in parallel events.
- The total angular distribution was approximated to be $\propto \cos^2(\theta)$ [3].
- The distance between the two levels is flexible in the detector. Two simulations were run, one with a distance of 20 cm, the other with a distance of 180 cm.
- The flux of parallel muon events was set to 1 m^{-2}s^{-1}. This number was chosen without any preference. The parallel flux was included in the total muon flux.

- In the event that a parallel event occurred, the probability for double, triple or quadruple muons was set to 0.6, 0.3 and 0.1 respectively. Again, these numbers were chosen arbitrarily.
- The maximum internal delay among the trigger cards was set to be 40 ns.
- The random noise to signal ratio was set to be 1:1. Because of the light leakage and electrical noise problems described in chapter 4, we had little means of knowing which channels would give noise and how large the noise ratio would be. Therefore, noise was distributed randomly in all channels
- In addition to random noise in all channels, 3 random channels were chosen and given extra noise with a noise to signal ratio of 1:1. This was done to take into account the possibility that some channels have more noise than the others. Again, the ratio and the channels chosen were random because we had no means of knowing how these parameters would be for the final setup.

We ran four different simulations of one hour each. Two were with a distance between the levels of 20 cm, and two with a distance of 180 cm. For each height, we ran one simulation without noise and one with noise.

The main structure of the simulation macro is a double *for*-loop. The first loop runs over the runtime in seconds, which is one of the arguments of the simulation macro. The second loop runs over all the time bins in each second. Since a time bin has a length of 100 ns, the second loop runs over 10^7 time bins for each second. For each time bin, a random float is generated between 0 and 10^7. If this number is smaller than the total flux parameter, it is interpreted as a hit in the first layer of the detector.

When there is a hit in the first layer, a random coordinate between 0 and 100 in the x-direction is generated. The time of the hit is placed randomly inside the time-bin. This time is given in ns. For the second layer, a random coordinate in the y-direction is generated. The time of the hit in the second layer is generated by adding a random number between -40 ns and $+40$ ns to the time of the hit in the first layer. The x- and y-coordinates are "translated" to channel numbers by a method in the CRTGeometry object and stored in an array. In the array, the index from 0-7 corresponds to channels 1-8. The times of the hits are then rounded up to the nearest time-bin (to the nearest multiple of 100 ns) and written in a separate time array. Since the trigger card signals in the detector are 200 ns, the simulated hits of both layers are read out in two adjacent time bins.

A hit in the first level generates random angles of the hit that follows a cosine square distribution, using a predefined class in ROOT called TF1. The angle $\theta \in [-\frac{\pi}{2}, \frac{\pi}{2}]$. An angle is generated separately for the x- and y-directions. The shift in level 2 compared with level 1 is then given by

$$\tan(\theta) = \frac{\Delta xy}{d} \leftrightarrow \Delta xy = d \cdot \tan(\theta) \tag{5.1}$$

where d is the distance between the levels and Δxy is the shift in either the x- or y-direction. The x- and y-coordinates of level 2 are then given as the coordinates of level 1 added the shift Δxy. If the coordinates are larger than 100 or smaller than 0, the muon missed level 2, and no hit is registered in the second level. If the coordinates are between 0 and 100, the corresponding channels are found in the same way as for the hits in level 1. A time of the hits is randomly generated for layer 3 and 4 in the same way as for layer 2. The time bins are also found in the same way.

All the angles that are generated in the simulation are plotted in a histogram. In addition, the angles corresponding to hits in both levels are plotted in a separate histogram. This is due to the fact that in the analysis and reconstruction, only muons hitting both levels can be reconstructed with an angular distribution. An example of the angles for the total and both level simulated muon hits are given in figure 5.1.

In addition to muon hits, the Simulation macro can also generate noise signals. The noise is generated in two ways. First, noise is generated in a random channel with an overall ratio of 1:1. Second, three channels are chosen at random and are given additional noise with a ratio of 5:1.

When the simulated muon has traversed the detector and/or noise signals have been generated, the simulated signals from all the channels and the corresponding time bins are written to file. The control bits are set to 0 in the simulation.

The data simulated in the Simulation macro give a higher hit rate for level 1 than for level 2. This is because of the way a muon hit is implemented in the simulation. A simulated muon always starts in the first level, and then continues either to hit or to miss the second level. Because of the angular distribution, many of the muons miss the second level. In the detector, an equal amount of real muons will miss the first level and hit the second level, giving approximately the same amount of hits in both levels. This fault in the simulation macro was deemed non-significant, since the primary function of the simulations was to create files with the correct structure.

5.4 CRTFileConverter Macro

The files created both by the Simulation macro and the readout of real data, most often records each event twice. This is because of the structure of the read-out described in chapter 3. The File Converter macro combines these duplicates to one event line and writes this to a new file, with the earliest time bin as time stamp. This file can then be read by the Analysis program. An example of running the CRTFileConverter is given in table 5.2

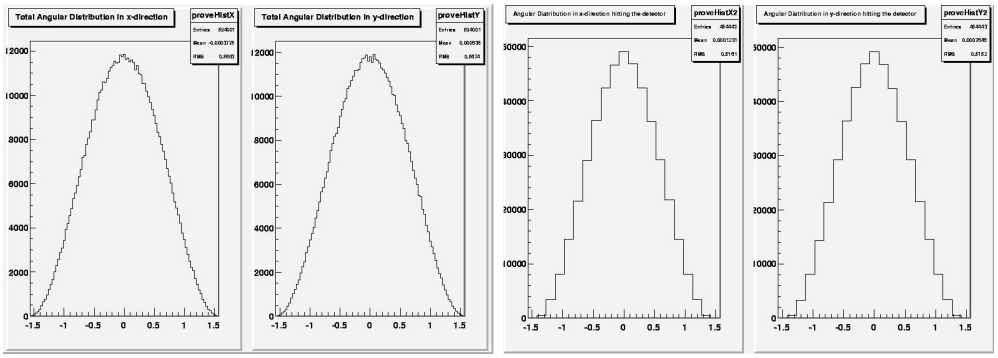

(a) Level distance 20 cm with noise: All muon angles generated.

(b) Level distance 20 cm with noise: Angles of all muons hitting within both levels.

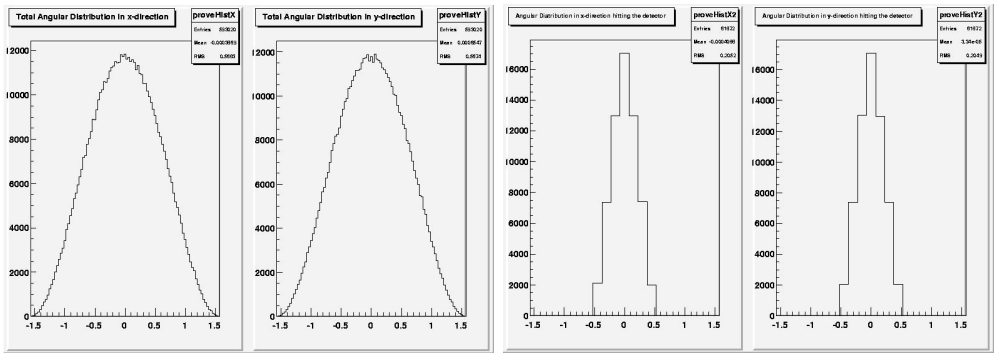

(c) Level distance 180 cm without noise: All muon angles generated.

(d) Level distance 180 cm without noise: Angles of all muons hitting within both levels.

Figure 5.1: Angle distributions in two one hour simulations at different level distances. The total angular distributions are the same with and without noise. The angular distribution of muons hitting both levels vary as the distance between the levels vary. The larger the distance, the better the angular distribution. The angles in x-direction are to the left, the y-direction to the right.

In	Out
0100010000100000 368309 0 0	0100010000100001 0 0 368309
0100010000100001 368310 0 0	
0000000000000001 368311 0 0	
0001001000000000 676150 0 0	0001001000000000 0 0 676150
0001001000000000 676151 0 0	

Table 5.2: Running the CRTFileConverter shifts the data of the "In"-column to data in the "Out"-column.

5.5 CRTanalysis Macro

The CRTanalysis macro reads the converted data files and plots several histograms displaying the muon rate, channel distribution, pad distribution and angular distribution. Several parameters from the data are also calculated.

5.5.1 Muon rate and flux

Muons traversing the detector can hit both levels or only one of the two. For this reason, to get a number for the flux, we have to look at the rates through each of the levels separately. We also have to consider the efficiencies of the levels in question. The muon rate R (muons per second) in each level is plotted in a 1D histogram with a bin size of 1 s. Muon rates of two simulated events are shown in figure 5.2.

The mean muon rate R is the number of events registered in a level N divided by the run-time t:

$$R = \frac{N}{t} \tag{5.2}$$

A muon event is defined as a coincidence event, i.e. a signal in both layers in a level in the same time bin.

The mean muon flux Φ through a level is given as the rate R divided by the efficiency of the level:

$$\Phi = \frac{R}{\epsilon_1 \cdot \epsilon_2} \tag{5.3}$$

where ϵ_1 and ϵ_2 are the efficiencies of the two layers making a level. Ideally, we would like to measure the efficiency of a level directly, but this is not possible due to the distance between the levels.

The efficiency of a layer ϵ_n can be calculated in two ways. The first is by looking at events in all four layers $\mathrm{N}_{1,2,3,4}$ divided by events in all layers accept the layer in question $\mathrm{N}_{1,2,3,4-n}$:

$$\epsilon_{n_1} = \frac{N_{1,2,3,4}}{N_{1,2,3,4-n}} \tag{5.4}$$

The other way of calculating layer efficiencies is by cross checking the number of events in a layer with the number of events in the opposite direction. We then look at the number of events in three layers ($\mathrm{N}_{n,1,3}$ or $\mathrm{N}_{n,2,4}$) divided by the number of events in the two layers that have the opposite direction of layer n ($\mathrm{N}_{1,3}$ or $\mathrm{N}_{2,4}$). For layer n in the x-direction, we get:

$$\epsilon_{n_2} = \frac{N_{n,2,4}}{N_{2,4}} \tag{5.5}$$

where $N_{2,4}$ are the number of events in the y-direction. The same is done for the layers in the y-direction. If we have no systematic errors, the two methods should give the same

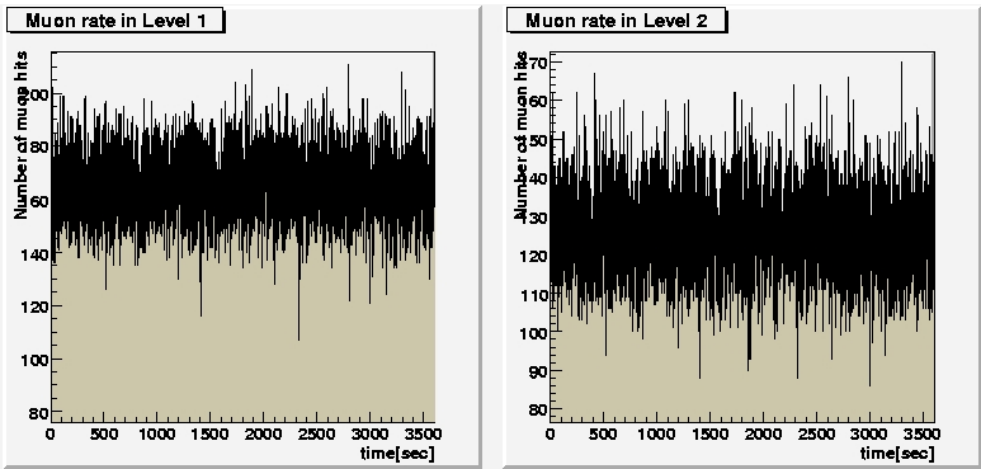

(a) Level distance 20 cm with noise: Muon rate in the two levels. $R_1 = \Phi_1 = 164.99 \pm .021$

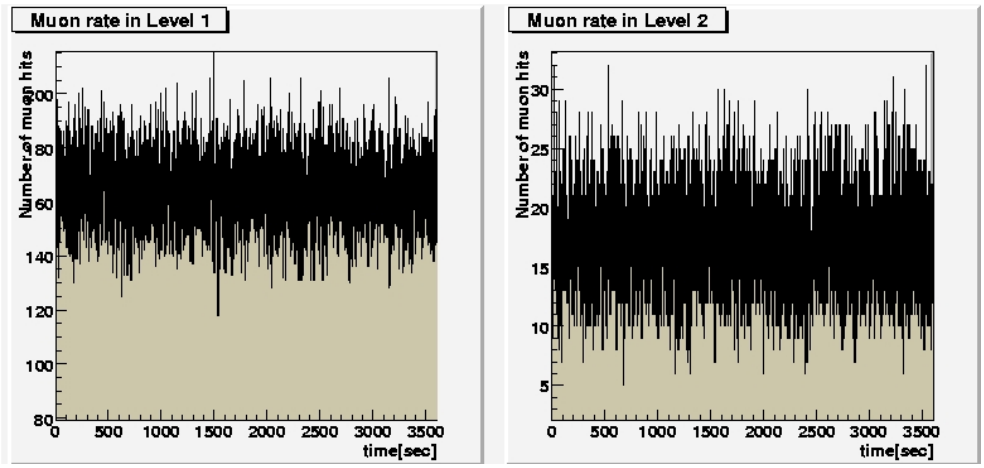

(b) Level distance 180 cm without noise: Muon rate in the two levels. $R_1 = \Phi_1 = 164.72 \pm 0.21$

Figure 5.2: The muon rate in level 1 and level 2 of the detector. Because of the fault of the simulation macro described above, the rates of the two levels are different.

values within statistical errors. As we have many events in the CRT, the statistical errors are of the order of 1 %.

In addition to the efficiencies of single layers, we also look at the efficiencies of two layers combined. These are given by:

$$\begin{aligned} \epsilon_{1,3} &= \frac{N_{1,2,3,4}}{N_{2,4}} \\ \epsilon_{2,4} &= \frac{N_{1,2,3,4}}{N_{1,3}} \\ \epsilon_{1,4} &= \frac{N_{1,2,3,4}}{N_{2,3}} \\ \epsilon_{2,3} &= \frac{N_{1,2,3,4}}{N_{1,4}} \end{aligned} \tag{5.6}$$

If we have no systematic errors, we should have the following relations between single layer efficiencies and efficiencies of two layers combined within the statistical errors:

$$\begin{aligned} \epsilon_{1,3} &= \epsilon_{1_1} \cdot \epsilon_{3_1} = \epsilon_{1_2} \cdot \epsilon_{3_2} \\ \epsilon_{2,4} &= \epsilon_{2_1} \cdot \epsilon_{4_1} = \epsilon_{2_2} \cdot \epsilon_{4_2} \\ \epsilon_{1,4} &= \epsilon_{1_1} \cdot \epsilon_{4_1} = \epsilon_{1_2} \cdot \epsilon_{4_2} \\ \epsilon_{2,3} &= \epsilon_{2_1} \cdot \epsilon_{3_1} = \epsilon_{2_2} \cdot \epsilon_{3_2} \end{aligned} \tag{5.7}$$

The statistical uncertainties in the muon rate and flux are given by a Poisson distribution:

$$\begin{aligned} \sigma_R &= \frac{\sqrt{N}}{t} \\ \sigma_\Phi &= \frac{\sqrt{N}}{t \cdot e_1 \cdot e_2} \end{aligned} \tag{5.8}$$

If the different methods of finding layer efficiencies give different values, we have systematic errors. Systematic errors are difficult to describe because we usually do not know why they occur. If the layer and two-layer efficiencies are different with the different methods, we can estimate the systematic error by subtracting the two values from each other:

$$\begin{aligned} \Delta\epsilon_n &= |\epsilon_{n_1} - \epsilon_{n_2}| \\ \Delta\epsilon_{n,m} &= \epsilon_{n,m_{\max}} - \epsilon_{n,m_{\min}} \end{aligned} \tag{5.9}$$

The flux is dependent on the layer efficiencies as shown in equation 5.3. Thus, if the efficiencies of the layers have systematic errors, this must be considered in the flux uncertainty as well. The relative statistical error for a function f of several variables $(a, b, ...)$ is given as

$$\frac{\Delta f}{f}_{\text{stat}} = \sqrt{\left(\frac{\Delta a}{a}\right)^2 + \left(\frac{\Delta b}{b}\right)^2 + ...} \tag{5.10}$$

With systematic errors, we do not know if they obey this equation. By comparing the two-layer efficiencies described in equation 5.7 with two and two single layer efficiencies multiplied, we can get an indication of the validity of using equation 5.10 for the systematic error.

In the simulation, all channels were set to function perfectly, giving all four layers an efficiency of 1 regardless of the methods described above. This in turn led to the muon rate of level 1 being equal to the muon flux. The rate and flux of level 2 differs from this due to the fault of the simulation macro.

5.5.2 Channel and noise distribution

The channel distribution (i.e. number of hits in each channel) of the signals registered in the detector are also plotted in a 1D histogram. The signals from muon hits are plotted together with the total number of signals in each channel. This is done to explore the noise rate of each of the 16 channels. Examples of simulated channel distributions with and without noise are given in figure 5.3.

5.5.3 Pad and angular distribution

In the analysis, each level in the CRT can be divided into 16 squares or pads. The number of hits in each pad is plotted for both levels. In this plot, only events with one muon are considered. By summing over all 16 pads, we can count the number of muon events in a level. An example is given in figure 5.4

Combining data from all four layers makes it possible to plot and to calculate a certain angular distribution. The resolution for a muon hitting a scintillator in both the x- and y-directions follows a box distribution. The resolution is given by

$$\sigma_{\text{box}} = \frac{d}{\sqrt{12}} = \frac{25\text{cm}}{\sqrt{12}} \approx 7.2\text{cm} \tag{5.11}$$

We do not know where in the scintillator a muon traverses, so in the angle reconstruction we place it in the middle of the width. With a distance between the layers of Z, the reconstructed angle is given by

$$\tan(\theta) = \left(\frac{xy_1 - xy_2}{Z}\right) \tag{5.12}$$

where xy is the center of the scintillator hit in either the x- or y-direction.

The angular resolution in both the x- and y-directions are given by

$$\sigma_{\tan(\theta)} = \left(\sqrt{\left(\frac{\Delta xy_1}{Z}\right)^2 + \left(\frac{\Delta xy_2}{Z}\right)^2}\right) = \left(\frac{\sqrt{2}}{Z}\frac{d}{\sqrt{12}}\right) \tag{5.13}$$

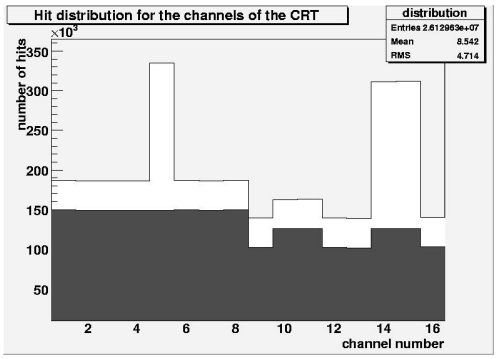

(a) Level distance 20 cm with noise: Signals (gray) and noise (white) in each channel

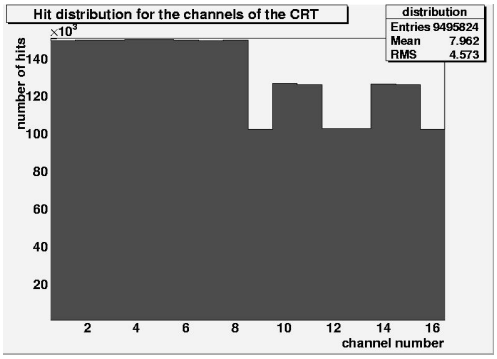

(b) Level distance 20 cm without noise: Signals (gray) in each channel

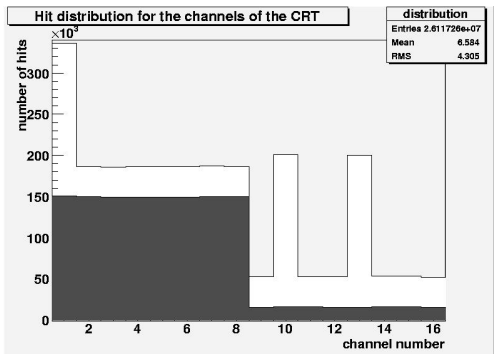

(c) Level distance 180 cm with noise: Signals (gray) and noise (white) in each channel

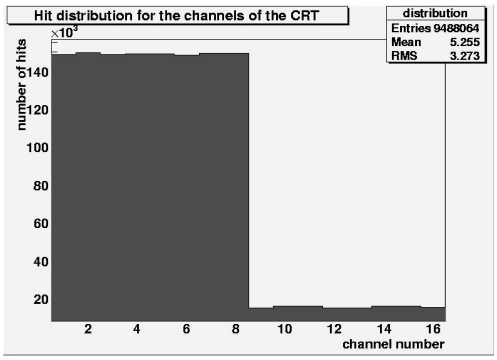

(d) Level distance 180 cm without noise: Signals (gray) in each channel

Figure 5.3: Number of muons and noise in each channel in various simulations. Notice that there is a higher hit-rate in the first level than the second, and that some of the channels in the second level have a higher hit rate than the others. This is due to the faulty of the simulation macro described above.

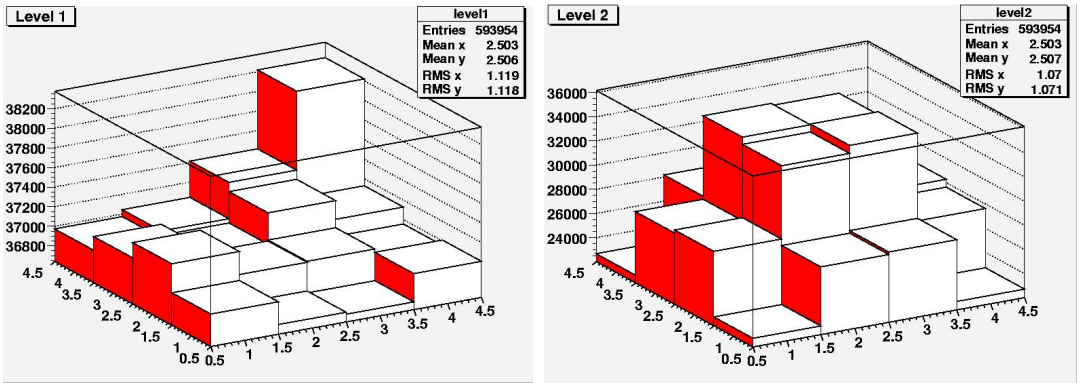

Figure 5.4: Number of muon hits in the pads of both levels of the CRT for a one hour simulation with level distance 20 cm. We see that the distribution in level 2 is not isotropic. This is, again, due to the faulty of the simulation macro. The pad distribution is similar for the other simulations.

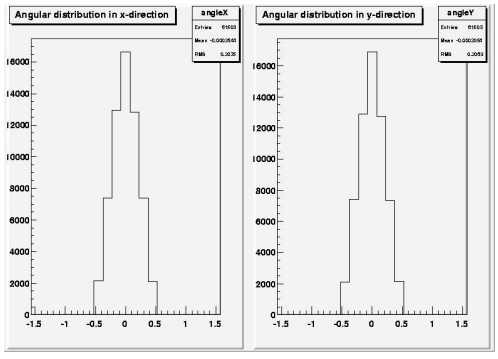

Figure 5.5: The reconstructed angular distribution of the simulation shown in figure 5.1(d)

The reconstructed angles are plotted in x- and y-direction respectively. An example of the angular distribution is given in figure 5.5.

If the efficiencies of the various layers differ from each other, this will effect the angular resolution.

5.5.4 Detection of parallel muons

A parallel event is defined as an event with hits in all four layers and at least two hits in one of the levels. In this case, if the muons are spaced so closely together that they hit the same scintillators in all four layers, the parallel event will be registered as a single muon hit. Since the total number of channels in each layer is 4, the maximum number of muons that can be registered is 4. A parallel event can thus consist of 2, 3 or 4 muons. The classification and possible mis-classification of parallel events is due to the large area of the pads. We have here omitted the possibility of using the angles of the muons to look at possible duplicates and/or double muons counted as one.

For each parallel event, the number of signals in each layer is registered. The layer with the most signals decides how many muons were in the parallel event. The parallel event rate R_{parallel} is the number of parallel events divided by the run-time t:

$$R_{\text{parallel}} = \frac{N_{\text{parallel events}}}{t} \tag{5.14}$$

The parallel event flux is given as the rate divided by the efficiency of all four layers combined. A few graphic examples of parallel events and channels activated are given in figure 5.6.

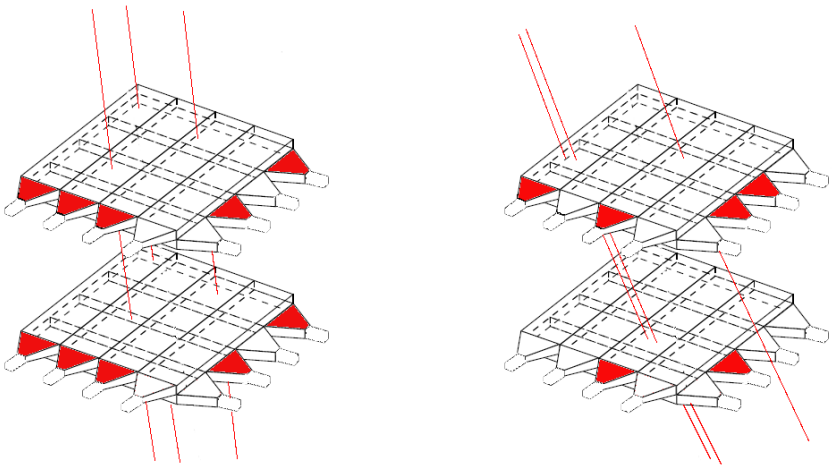

(a) An event where all the muons hit separate scintillators in at least one layer.

(b) An event where two of the muons are registered as one because they hit the same scintillators in all four layers.

Figure 5.6: Two examples of what a parallel event could look like. Red color on a light guide indicates that a count is registered from the channel.

Chapter 6

First Data Analysis with CRT

The noise problems described in chapter 4 gave data with only some of the channels functioning. Due to lack of time, further tuning of the detector was omitted. Two data runs were commenced, a half hour run November 5^{th} (labeled "20071105") and a one hour run November 6^{th} (labeled "20071106"). The level distance Z was 70 cm. Analysis was carried out on the data from these two runs.

6.1 Layer efficiencies and errors

In order to say something about the data taken, it was important to first determine if there were any systematic errors. The different single- and two-layer efficiencies for the two data-sets, calculated using the equations described in chapter 5, are summarized in table 6.1. The statistical error of the efficiencies is of the order of 1%. We see that the efficiencies for single layers differ, as well as the efficiencies of two layers combined. We have systematic errors of unknown origin. We want to determine if the combined layer efficiencies seem to follow equation 5.10. This is done by comparing the relative errors of two layers combined using equation 5.9 with the errors found using equation 5.10. The results of these calculations are given in table 6.2.

The two methods of calculating two-layer efficiency errors do not give the same results. We have to conclude that using the statistical equation 5.10 is not possible to determine the error in the level efficiencies $\epsilon_1 \cdot \epsilon_2$ and $\epsilon_3 \cdot \epsilon_4$. Using equation 5.9 we get level efficiencies and corresponding errors given in table 6.3.

We could also have calculated the efficiencies of single channels. This would have given yet another measure of the detector's efficiencies, but was omitted due to a lack of time. Also, improvements in the setup would give better efficiencies.

As a concluding remark on the efficiency discussion, we cannot say why we are experiencing systematic errors in the layer efficiencies. We have also seen that the systematic errors do not follow the statistical formula to combine them. The largest differences in two-layer efficiencies calculated above indicate a systematic error in the level efficiencies of the order of 20 %.

	20071105	20071106
ϵ_{1_1}	0.527	0.512
ϵ_{2_1}	0.747	0.731
ϵ_{3_1}	0.354	0.366
ϵ_{4_1}	0.409	0.400
ϵ_{1_2}	0.539	0.526
ϵ_{2_2}	0.792	0.786
ϵ_{3_2}	0.362	0.376
ϵ_{4_2}	0.434	0.430
$\epsilon_{1_1} \cdot \epsilon_{3_1}$	0.186	0.188
$\epsilon_{2_1} \cdot \epsilon_{4_1}$	0.306	0.292
$\epsilon_{1_1} \cdot \epsilon_{4_1}$	0.216	0.205
$\epsilon_{2_1} \cdot \epsilon_{3_1}$	0.264	0.268
$\epsilon_{1_2} \cdot \epsilon_{3_2}$	0.195	0.198
$\epsilon_{2_2} \cdot \epsilon_{4_2}$	0.344	0.338
$\epsilon_{1_2} \cdot \epsilon_{4_2}$	0.234	0.226
$\epsilon_{2_2} \cdot \epsilon_{3_2}$	0.287	0.296
$\epsilon_{1,3}$	0.191	0.193
$\epsilon_{2,4}$	0.324	0.314
$\epsilon_{1,4}$	0.192	0.180
$\epsilon_{2,3}$	0.251	0.259

Table 6.1: Single- and double layer efficiencies calculated using different methods.

	20071105	20071106
$\Delta\epsilon_1$	0.013	0.014
$\Delta\epsilon_2$	0.045	0.055
$\Delta\epsilon_3$	0.0084	0.0098
$\Delta\epsilon_4$	0.025	0.030
$\frac{\Delta\epsilon_{1,3}}{\epsilon_{1,3}}$	0.047	0.053
$\frac{\Delta\epsilon_{2,4}}{\epsilon_{2,4}}$	0.12	0.15
$\frac{\Delta\epsilon_{1,4}}{\epsilon_{1,4}}$	0.20	0.22
$\frac{\Delta\epsilon_{2,3}}{\epsilon_{2,3}}$	0.14	0.14
$\frac{\Delta\epsilon_{1,3}}{\epsilon_{1,3}}_{\text{ stat}}$	0.033	0.037
$\frac{\Delta\epsilon_{2,4}}{\epsilon_{2,4}}_{\text{ stat}}$	0.082	0.10
$\frac{\Delta\epsilon_{1,4}}{\epsilon_{1,4}}_{\text{ stat}}$	0.063	0.077
$\frac{\Delta\epsilon_{2,3}}{\epsilon_{2,3}}_{\text{ stat}}$	0.063	0.077

Table 6.2: Single- and double layer efficiency errors. The double-layer systematic errors are calculated in two ways described in the text.

	20071105	20071106
$\epsilon_{1_1} \cdot \epsilon_{2_1}$	0.393	0.374
$\epsilon_{3_1} \cdot \epsilon_{4_1}$	0.145	0.146
$\epsilon_{1_2} \cdot \epsilon_{2_2}$	0.427	0.413
$\epsilon_{3_2} \cdot \epsilon_{4_2}$	0.157	0.162
$\frac{\Delta\epsilon_{1,2}}{\epsilon_{1,2}}$	0.082	0.099
$\frac{\Delta\epsilon_{3,4}}{\epsilon_{3,4}}$	0.082	0.099

Table 6.3: Level efficiencies and corresponding errors

6.2 Signal and noise distribution

The plot showing signal and noise ratios in all the channels gives a good impression of which channels function well, and which that do not. The plot shows the number of muon- and noise signals in each channel in the entire run time. The signal and noise distributions of the two data-sets are shown in figure 6.1.

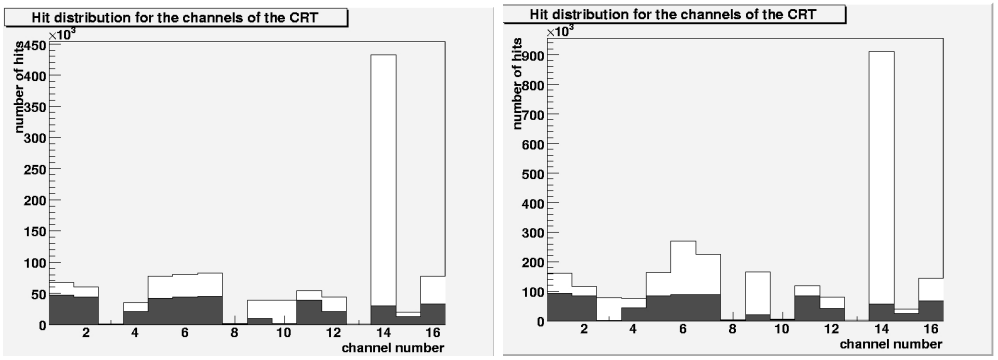

(a) 20071105: Signals (gray) and noise (white) in each channel

(b) 20071106: Signals (gray) and noise (white) in each channel

Figure 6.1: Total number of muons and noise in each channel.

From the distribution plots we see that the two data-sets are consistent with each other. This is also confirmed by looking at the various parameters extracted from the data described below. With all the problems described in chapter 4, it is reassuring to see that the detector at least seems to be working in the same way on two different occasions.

The most striking features of the distribution are the large variations among the channels. We see that all channels have some noise, but the better part of the total noise is due to the large noise rate in channel 14. Apparently, this channel has exceed it's stability level, as we observed that it could do while turning down the voltage (table 4.5). Channel 13 is off, while channels 3, 8 and 10 have a much lower signal rate than the others. In addition, channels 4, 9, 12 and 15 have a lower rate than the remaining channels.

	20071105	20071106
$N_{1,2}$	101227	199060
$N_{3,4}$	48813	99550
Rate Level 1 [Hz]	55.86 ± 0.18	54.93 ± 0.12
Flux Level 1[$s^{-1}m^{-2}$]	136.2 ± 20%	139.5 ± 20%
Rate Level 2 [Hz]	26.93 ± 0.12	27.47 ± 0.09
Flux Level 2[$s^{-1}m^{-2}$]	178.4 ± 20%	178.3 ± 20 %

Table 6.4: Muon rates and fluxes. $N_{1,2}$ is the number of events in level 1, and $N_{3,4}$ is the number of events in level 2.

In addition to plotting the total number of signals in each channel, we also plot the relative number of muons in each channel compared to the channel with the most hits. This gives an impression of the relative efficiencies of the various channels. For the two data-sets, these plots are shown in figure 6.2.

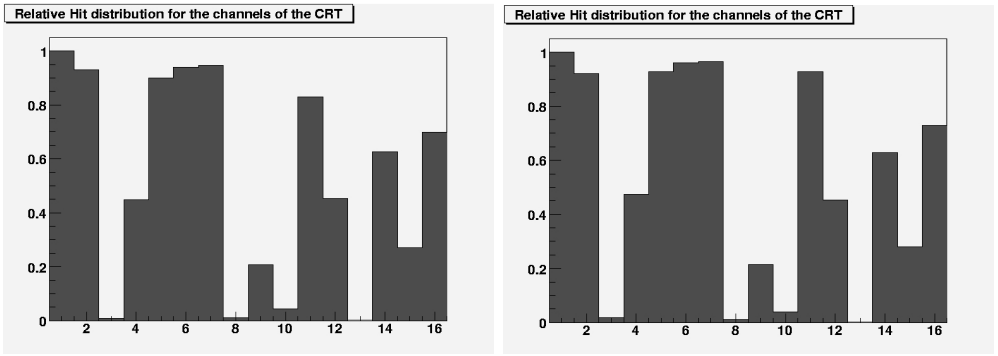

(a) 20071105: Relative muon number *(b)* 20071106: Relative muon number

Figure 6.2: The relative muon number in each channel.

6.3 Muon rate and flux

The muon rate through each level is plotted as a function of the time. The rate distributions for the two data-sets are shown in figure 6.3.

The mean rates and fluxes of the two levels are calculated using equations 5.2 and 5.3. In the flux calculation, the systematic efficiency errors derived above are include. The statistical errors are negligible compared to the systematic errors. A summary of the muon rates and fluxes are given in table 6.4.

The number of parallel events and the corresponding parallel rates and fluxes are given in table 6.5. As the parallel flux is dependent on the efficiencies of both levels, the systematic error of both levels combined must be considered.

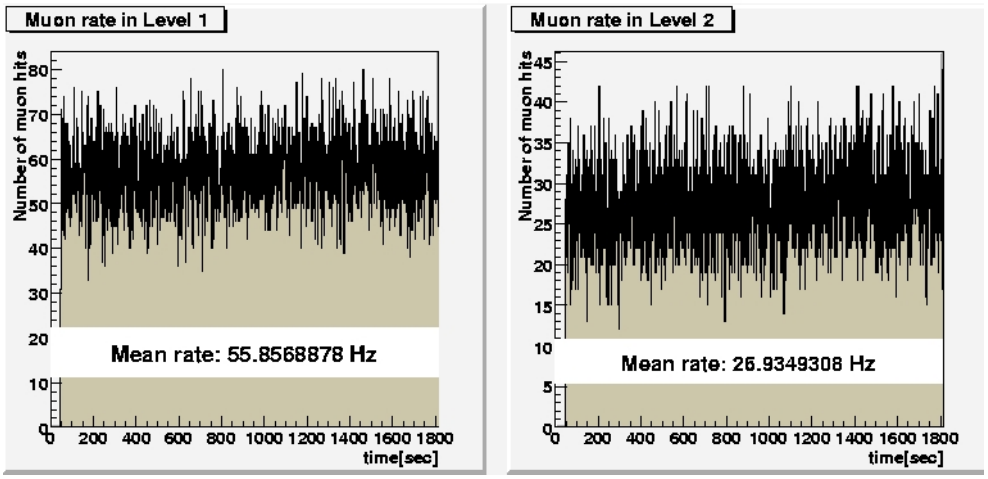

(a) 20071105: Muon rate in the two levels.

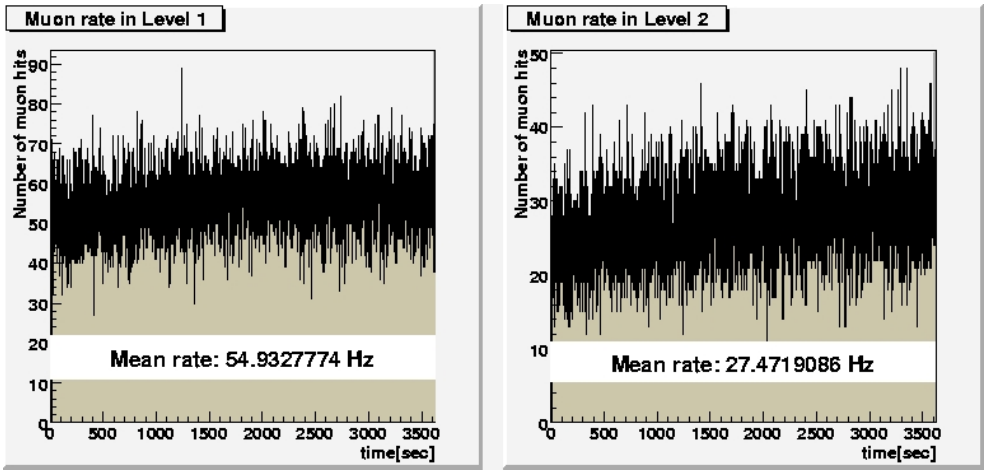

(b) 20071106: Muon rate in the two levels.

Figure 6.3: Muon rates.

	20071105	20071106
$N_{parallel}$	328	607
Rate[Hz]	0.18 ± 0.01	0.168 ± 0.007
Flux[$s^{-1}m^{-2}$]	2.9 ± 40 %	2.8 ± 40 %

Table 6.5: Parallel muon rates and fluxes.

6.4 Pad distribution and angular distribution

The pad distributions for the two data-sets are shown in figure 6.4.

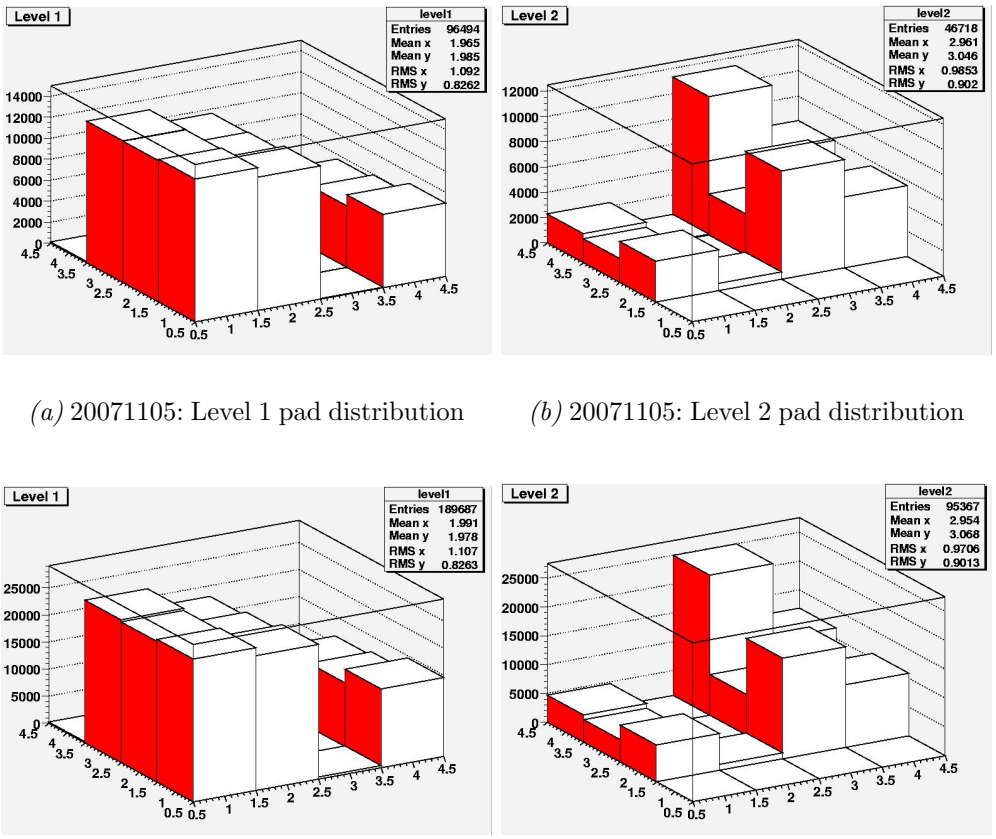

(a) 20071105: Level 1 pad distribution *(b)* 20071105: Level 2 pad distribution

(c) 20071106: Level 1 pad distribution *(d)* 20071106: Level 2 pad distribution

Figure 6.4: Pad distributions.

Summing over all 16 pads, we get the total number of muon events through level 1 and 2. The corresponding rates and fluxes are given in table 6.6.

Due to the low efficiencies of many of the channels, the readout was asymmetric. As a result, the angular distribution of the muons is asymmetric. This plot could be corrected, but it would demand a calculation of the single channel efficiencies. A plot of the asymmetric angle distribution for both data-sets is shown in figure 6.5.

	20071105	20071106
$N_{1,2}$	96494	189687
$N_{3,4}$	46718	95367
Rate Level 1 [Hz]	53.25 ± 0.17	52.35 ± 0.12
Flux Level 1[$s^{-1}m^{-2}$]	129.8 ± 20%	133.0 ± 20%
Rate Level 2 [Hz]	25.78 ± 0.12	26.32 ± 0.09
Flux Level 2[$s^{-1}m^{-2}$]	170.7 ± 20%	170.8 ± 20 %

Table 6.6: Muon rates and fluxes using the sum over the pads of a level.

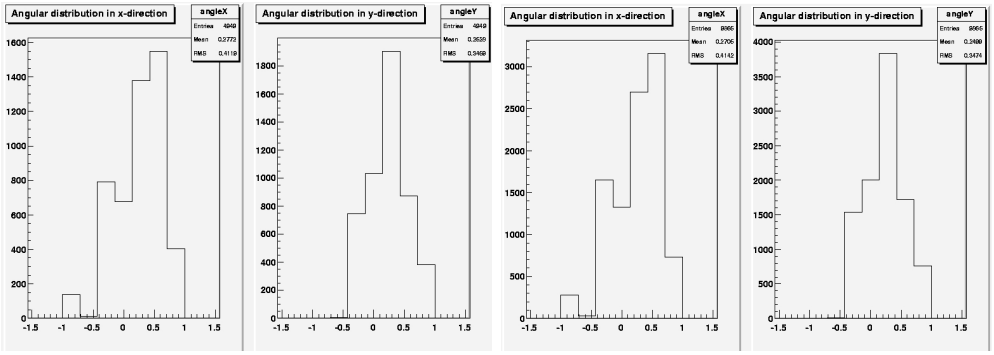

(a) 20071105: Angular distribution in x- and y-directions.

(b) 20071106: Angular distribution in x- and y-directions.

Figure 6.5: Angular distributions. The x-direction to the left and y-direction to the right.

Chapter 7

Future projects

The first data taken with the CRT have been analyzed to find muon rates and fluxes, noise ratios and angular distribution through the detector. Further tuning of the detector and possibly replacement of several of the PMTs will be necessary to increase the efficiencies and reduce the systematic errors for the detector. This must be done before future projects are initialized. Modifications to the setup can allow the measuring of additional muon properties. If several simplified detectors are constructed and timed together, it is possible to use the CRT as one of many detectors in a detector array. Some of the possibilities for future projects are described in the following sections.

7.1 Parallel Events

In the first data analysis, the parallel events were neglected in the angular distribution. If the parallel events are included in the angular distribution, this can give better statistics. In addition, it is possible that parallel muons can hit one level each, thus allowing more than four muons to be registered in one parallel event. This can be deducted by looking more carefully at the parallel events. An example of such an event is given in figure 7.1

7.2 Measurement of the muon lifetime and parity violation

To measure the muon lifetime, the initial setup must be modified. In the space between the two levels, an aluminum plate is inserted. When a muon hits the aluminum plate, it is slowed down due to the higher density of aluminum compared to air. Initially, the muons can reach Earth because of time dilation as explained in chapter 2. When a muon hits the aluminum plate, it can be slowed down enough to decay. As described in chapter 2, a muon decays into an electron, a muon neutrino and an electron anti-neutrino. Because the primary cosmic radiation is dominated by protons, the ratio between anti-muons and muons is between 1.1 and 1.4 [3].

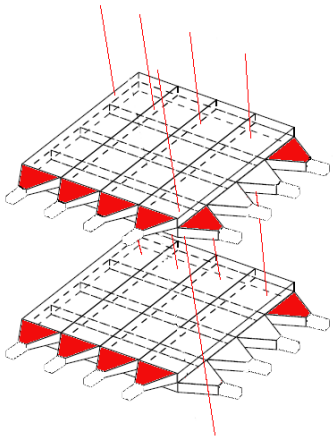

Figure 7.1: An example of a parallel event where more than 4 muons are registered and can be deducted from analysis. By looking at the similarities and differences in hits in the two levels, we can reconstruct the four muons in the back row and the single muon in the foreground. This demands a much more thorough investigation of the parallel events than what was the case in our analysis.

Anti-muons hitting matter can traverse the matter or decay due to deceleration. Muons, since they carry negative charge, have one more possibility. After deceleration, they can be captured by a nucleus in so-called Bohr orbits. Because of this, the negative component of the cosmic muons disappears faster than the positive component. In the following, we will therefore look at anti-muons.

As described in chapter 2, muons are polarized in the pion-decay. Thus, the incoming muons are polarized. To measure the lifetime of the anti-muon, we have to look for hits in one level followed by a hit in the other level only a short time after. In addition, the angle with which the anti-muons decay, should be isotropic if we did not have parity violation. By magnetizing the aluminum, this angular distribution is replaced by a time distribution. By looking at asymmetries in the time distribution, we can detect parity violation in the muon decay.

7.3 Flux variations compared to the solar weather

In chapter 2, we mentioned that the cosmic ray flux over larger periods of time is partly dependent on the solar weather. By taking data from the CRT over several days, even weeks, and then plotting the flux over this period, we can study fluctuations in the flux. These can then be compared to variations in the solar activity.

7.4 Detection of very high energy cosmic ray showers

The CRT can also be used as one of many detectors in an array or system of detectors. Several possibilities for an array system exist. The most appealing and also the most theasible solution is making several smaller detectors and placing them in various locations in the vicinity of the CRT. These smaller detectors will look very similar to the PMT test setup described in chapter 4, and register muons as double or triple coincidences in two or three scintillators on top of each other.

The array of detectors is dependent on getting exact timing correlated between the different detectors in the array. To achieve this correlation, it is necessary to use a precise mutual timing system, for instance GPS. This in turn demands a modification of the CRT both in the hardware and the software.

The basic idea of the detector array is registering the radius of a shower induced by a primary cosmic ray. The radius of the shower increases with increasing primary cosmic ray energy. The project of making the additional detectors is planned to be a cooperation with various high schools in the Bergen area. By involving high school students in the project, we can involve them in subatomic physics in a much more thorough way than is normally the case. In this way, the project will also be a means to introduce our field of physics to potential students.

Chapter 8

Conclusion

In this thesis, we have described the Cosmic Ray Telescope and the completion of it's construction. The construction and implementation of the analysis program has been the main part of the thesis. Data-taking has been initiated. In the process of constructing and testing the detector, one major mis-assumption was made, namely that the PMTs had a high noise rate due to light leakage alone. Combined with running the PMTs at higher voltages than they probably were constructed for, this led to a high electrical noise rate in the final setup. In addition, several of the PMTs did not function efficiently. The faults were unresolved due to lack of time. Further fine-tuning and possible PMT replacements will be necessary to get the detector's efficiency to an acceptable level.

The first data taken with the CRT have been analyzed to retrieve the mean muon flux. Due to large, unresolved systematic errors in the efficiencies of the detector layers, the mean flux measurements have a large error, and also vary with different methods for counting muons. The cause of these systematic errors are unknown. The fluxes calculated are in agreement with other measurements within the error.

Appendix A

CRT operating and analysis instructions

Operating the CRT and analyzing the data is a multi-step process. It is described in the following section.

A.1 Power on

1. Before the power is turned on, the door of the light-proof tent must be closed. It is also important to keep it closed as long as the PMTs are turned on.
2. Turn on the two laboratory power supplies powering the trigger cards and the read-out card. The trigger cards are supplied with one 24 V and one 5 V input, while the read-out card is supplied with 5 V.
3. Turn on the four red switches on the lower right side of the control panel(turning on the computer power supplies in the four layers). Red lights indicate if these supplies are on. Then, turn on the 16 black switches to the left of these (turning on the power to the HV-cards). Green lights indicate if these channels are on. The channels corresponding to the different switches are given in figure A.1.
4. Wait at least 15 minutes for the PMTs and trigger cards to stabilize

The CRT is now ready for data acquisition.

A.2 Data acquisition

The data acquisition program is made in LabVIEW. It is comprised of two parts; a readout program and a command program. Data acquisition is commenced in the following way:

1. Open “CRTReadout.vi” and “CRTSendCommand.vi”. The two programs’ interfaces are shown in figure A.2.

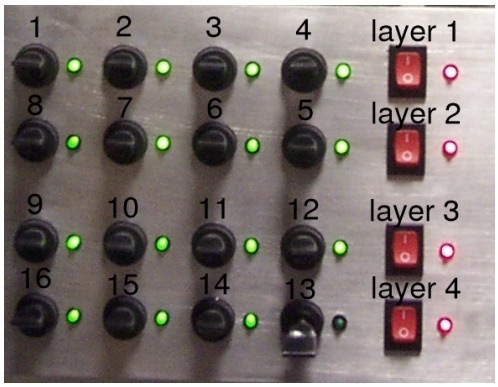

Figure A.1: PMT HV-card switches and corresponding channel numbers.

2. In "CRTReadout.vi", press the start button (white arrow in the upper left-hand corner). Enter the name of the data file to which the data are to be written. Typical format: <date and time>.txt. The readout program is now standing by.
3. To activate the readout from the FPGA, we use the "CRTSendCommand.vi" program. On the right-hand side of the interface, there is a vertical row of command buttons with the label "kommando" above. The top five commands are initialized, and have the following functions:
   - Calibration trigger: The FPGA reads the 16 channels, and returns a 1 in the calibration bit column
   - FIFO out clear: If the FIFO is full, this command clears the FIFO, and returns a data string with a 1 in the FIFO full column
   - Stop: Stops the FPGA readout
   - Start: Starts the FPGA readout
   - Clock reset: Resets the internal clock
4. The readout is started by clicking on the "Start" command described above, and then pressing the start button for the "CRTSendCommand.vi" interface (the button marked "Send" is uninitialized and is not used). In the "CRTReadout.vi" window, we should now see data strings in the central area labeled "String".
5. The readout is stopped by clicking on the "stop" command in the "CRTSendCommand.vi" window (and un-clicking the "start" command) and then pressing the start button. The data acquired are now stored in a file.
6. Stop the "CRTReadout.vi" by pressing the "Stop" button on the left side in the interface.

A.3 Data analysis

The data file can be analyzed to get the various parameters and plots described in chapter 5. To achieve this, two ROOT macros are needed; "CRTFileConverter.cpp" and "CRT-analysis.cpp". In addition, the class "CRTGeometry" is needed. The class consists of the

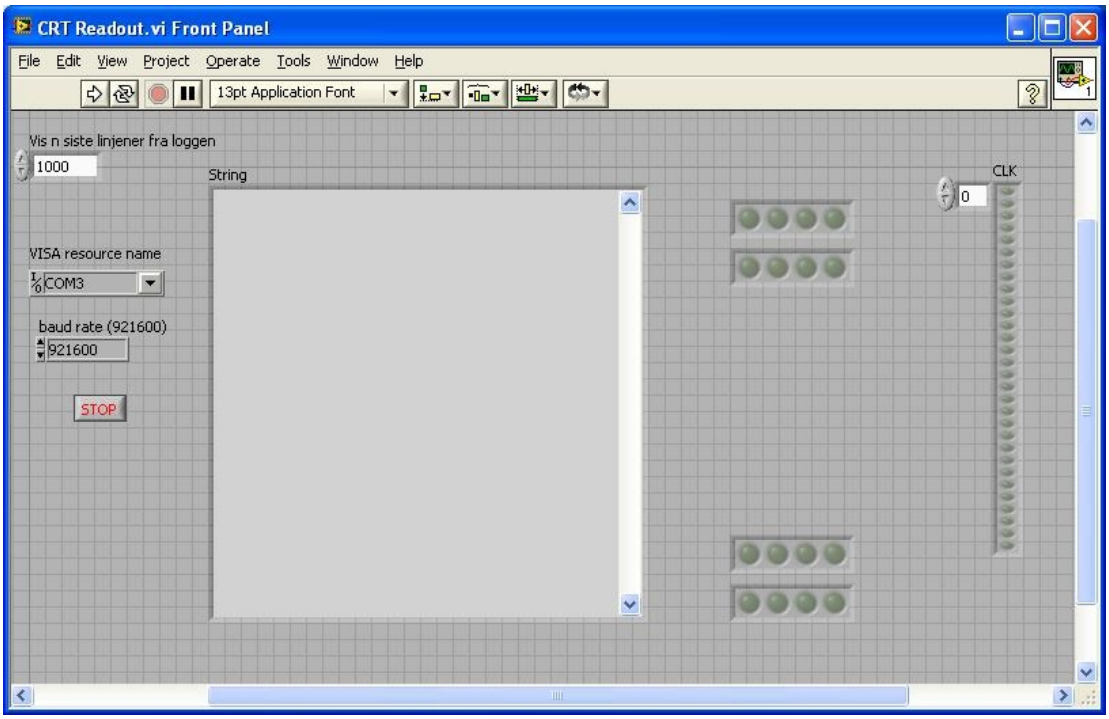

(a) CRTReadout.vi interface

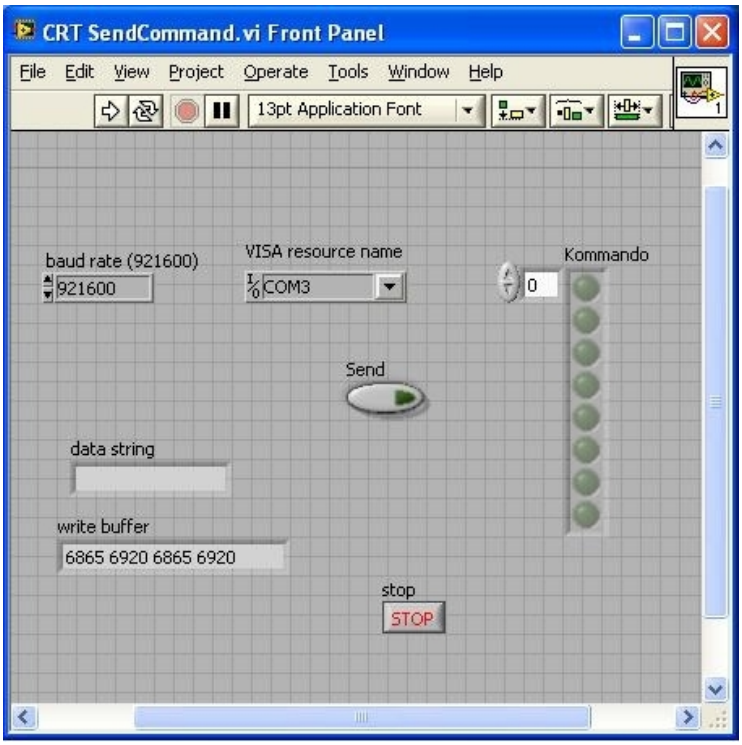

(b) CRTSendCommand.vi interface

Figure A.2: LabVIEW programs' interfaces.

files “CRTGeometry.cxx” and “CRTGeometry.h”. The data file is analyzed in the following way:

1. Open ROOT in a terminal. Compile the four files mentioned above. This is done by typing the following (in this order):
   - .L CRTGeometry.cxx+
   - .L CRTGeometry.h+
   - .L CRTFileConverter.cpp+
   - .L CRTanalysis.cpp+
2. In the data file, most events are written twice as described in chapter 3. These duplicates are merged into one using the CRTFileConverter by typing: .x CRTFileConverter.cpp+ (“<datafile in>.txt”,”<converted file out>.txt”)
3. The converted file can now be analyzed using the CRTanalysis macro. The parameters derived are printed to a file <results>.txt. The CRTanalysis macro is activated by typing: .x CRTanalysis.cpp+ (“<converted file>.txt”, “<results>.txt”).

The files “CRTFileConverter.cpp”, “CRTanalysis.cpp”,“CRTGeometry.cxx” and “CRTGeometry.h” are included as an attachment to the thesis.

Bibliography

[1] F. Close. *Particle Physics - A Very Short Introduction*. Oxford Universtiy Press, 2004.

[2] H. Frauenfelder and E. M. Henley. *Subatomic Physics*. Prentice-Hall Inc., 1991.

[3] W.-M.et al. Yao. Review of Particle Physics. *Journal of Physics G*, 33:1+, 2006.

[4] B.R. Martin and G. Shaw. *Particle Physics*. John Wiley & Sons, 1992.

[5] Y. Fukuda et al. Evidence for oscillation of atmospheric neutrinos. *PHYSICAL REVIEW LETTERS*, 1998.

[6] P.C. Hemmer. *Kvantemekanikk*. Tapir akademiske forlag, 2005.

[7] F. Mandl and G. Shaw. *Quantum Field Theory*. John Wiley & Sons, 1993.

[8] E. v.P. Smith and K.C. Jacobs. *Introductory Astronomy and Astrophysics*. W.B. Saunders Company, 1973.

[9] N. F. Comins and W. J. Kaufmann III. *Discovering the Universe*. W. H. Freeman and Company, 2005.

[10] Swordy Cronin, Gaisser. Cosmic rays at the energy frontier. *Scientific American*, 1997.

[11] P. Hofverberg. *Imaging the High Energy Cosmic Ray Sky*. PhD thesis, KTH Engineering Sciences, 2006.

[12] E. Chaisson and S. McMillan. *Astronomy - A Beginner's Guide to the Universe*. Pearson Prentice Hall, 2007.

[13] Todor Stanev. *High Energy Cosmic Rays*. Springer, 2004.

[14] G. Battistoni and A.F. Grillo. Introduction to high energy cosmic ray physics. 1995.

[15] K. Greisen. End to the cosmic ray spectrum? *PHYSICAL REVIEW LETTERS*, 1966.

[16] M. Takeda N. Sakaki M. Teshima T. Yamamoto, K. Mase. Signatures of ultra-high energy cosmic ray composition from propagation of nuclei in intergalactic photon fields. *Astroparticle Physics*, 2004.

[17] Wilkinson Microwav Anisotropy Probe (WMAP) web page. http://map.gsfc.nasa.gov/.

[18] D.N. Schramm and C.T. Hill. Origin of the ultra-high-energy cosmic rays. *FERMILAB-CONF-83*, 1983.

[19] Dick R. Blasi, P. and E.W. Kolb. Ultra-high energy cosmic rays: The annihilation of super-heavy relics. *Nuclear Physics B*, 2002.

[20] Pierre Auger Observatory web page. http://www.auger.org/.

[21] . Holter A. Egeland and A. Omholt. *Cosmical Geophysics*. Universitetsforlaget, 1973.

[22] K. Kleinknecht. *Detectors for Particle Radiation*. Cambridge University Press, 1998.

[23] Magne Munkjord. Developement of the ALICE busy box. Master's thesis, University of Bergen, 2007.

[24] Wikipedia Mylar page. http://en.wikipedia.org/wiki/mylar.
[25] Wikipedia ROOT page. http://en.wikipedia.org/wiki/root.